Spinor *GW*/Bethe-Salpeter calculations in BerkeleyGW: Implementation, symmetries, benchmarking, and performance

Bradford A. Barker,[1,2,3,*] Jack Deslippe,[4] Johannes Lischner,[5] Manish Jain,[6] Oleg V. Yazyev,[7] David A. Strubbe,[3] and Steven G. Louie[1,2]

[1]*Department of Physics, University of California, Berkeley, Berkeley, California 94720, USA*
[2]*Materials Sciences Division, Lawrence Berkeley National Laboratory, Berkeley, California 94720, USA*
[3]*Department of Physics, University of California, Merced, Merced, California 95343, USA*
[4]*National Energy Research Scientific Computing Center, Lawrence Berkeley National Laboratory, Berkeley, California 94720, USA*
[5]*Department of Materials and Physics, and Thomas Young Centre for Theory and Simulation of Materials, Imperial College London, London SW7 2AZ, United Kingdom*
[6]*Center for Condensed Matter Theory, Department of Physics, Indian Institute of Science, Bangalore 560012, India*
[7]*Institute of Physics, Ecole Polytechnique Federale de Lausanne (EPFL), CH-1015 Lausanne, Switzerland*

(Received 28 May 2022; revised 25 August 2022; accepted 6 September 2022; published 15 September 2022)

Computing the *GW* quasiparticle band structure and Bethe-Salpeter equation (BSE) absorption spectra for materials with spin-orbit coupling have commonly been done by treating *GW* corrections and spin-orbit coupling (SOC) as separate perturbations to density-functional theory. However, accurate treatment of materials with strong spin-orbit coupling (such as many topological materials of recent interest, and thermoelectrics) often requires a nonperturbative approach using spinor wave functions in the Kohn-Sham equation and *GW*/BSE. Such calculations have only recently become available, in particular for the BSE. We have implemented this approach in the plane-wave pseudopotential *GW*/BSE code BerkeleyGW, which is highly parallelized and widely used in the electronic-structure community. We present reference results for quasiparticle band structures and optical absorption spectra of solids with different strengths of spin-orbit coupling, including Si, Ge, GaAs, GaSb, CdSe, Au, and Bi_2Se_3. The calculated quasiparticle band gaps of these systems are found to agree with experiment to within a few tens of meV. SOC splittings are found to be generally in better agreement with experiment, including quasiparticle corrections to band energies. The absorption spectrum of GaAs is not significantly impacted by the inclusion of spin-orbit coupling due to its relatively small value (0.2 eV) in the Λ direction, while the absorption spectrum of GaSb calculated with the spinor *GW*/BSE captures the large spin-orbit splitting of peaks in the spectrum. For the prototypical topological insulator Bi_2Se_3, we find a drastic change in the low-energy band structure compared to that of DFT, with the spinorial treatment of the *GW* approximation correctly capturing the parabolic nature of the valence and conduction bands after including off-diagonal self-energy matrix elements. We present the detailed methodology, approach to spatial symmetries for spinors, comparison against other codes, and performance compared to spinless *GW*/BSE calculations and perturbative approaches to SOC. This work aims to spur further development of spinor *GW*/BSE methodology in excited-state research software and enables a more accurate and detailed exploration of electronic and optical properties of materials containing elements with large atomic numbers.

DOI: 10.1103/PhysRevB.106.115127

I. INTRODUCTION

Solid state physics and materials research is increasingly focusing its attention on materials containing heavy elements. Such materials have large spin-orbit coupling, often exceeding 1 eV for atoms from the fifth and sixth rows of the periodic table. These materials are important as thermoelectrics [1–8] and also can be topological insulators [9–17] and Weyl semimetals [18–21], among other novel topological phases [22–24]. Hybrid organic metal halide perovskite materials are also of great interest for photovoltaics, and contain heavy elements such as Pb, I [25], and/or Bi [26], and spin-orbit effects like Rashba splitting can play a role in their optical properties [27]. The standard approach to investigating the ground state electronic structure of these materials is density functional theory (DFT) [28,29]. Despite its widespread use to compute band structures, it is important to note that the Kohn-Sham eigenvalues of DFT do not have a rigorous physical meaning apart from the energy of the highest occupied molecular orbital, resulting in the well-known band gap problem of DFT. To compute excited-state properties such as band structures and absorption spectra, one must go beyond DFT and use many-body perturbation theory approaches, such as the *GW* [30,31] and *GW*/BSE methods [32].

The Dirac equation gives the relativistic quantum mechanical description of a fermionic wave function and yields four-component bispinor solutions. However, an expansion

*bbarker6@ucmerced.edu

of the Dirac equation to first order in c^{-2} yields the usual Schrödinger equation plus three additional terms [33]. For a system with N ions and n electrons, within the Born-Oppenheimer approximation, these terms are

$$H^{\mathrm{rel}} = -\sum_{\mathrm{i,I}}^{n,N} \frac{1}{8m_e^2c^2}\nabla_{\mathrm{i}}^2 V_{\mathrm{I}}(\mathbf{r}_{\mathrm{i}}) - \sum_{\mathrm{i}}^{n} \frac{\nabla_{\mathrm{i}}^4}{8m_e^3c^2} - \sum_{\mathrm{i,I}}^{n,N} \frac{e^2}{2m_e^2c^2}\mathbf{S}\cdot\mathbf{p}_{\mathrm{i}} \times \nabla_{\mathrm{i}}(V_{\mathrm{I}}(\mathbf{r}_{\mathrm{i}})), \quad (1)$$

the Darwin, relativistic mass correction, and spin-orbit coupling terms, respectively. We use $V_{\mathrm{I}}(\mathbf{r}_{\mathrm{i}})$ to denote the potential from ion "I" for electron "i." For valence electrons in nonhydrogenic atoms, SOC scales as Z^2 [34,35].

One should use such a "fully relativistic" treatment for materials with sufficiently large Z, starting with the calculation of the two-component spinor Kohn-Sham states and then using these states to calculate excited-state properties, such as the quasiparticle band structure and the absorption spectrum. This first-principles method also allows for capturing the effect of the renormalization of the spin-orbit coupling strength [36], along with improved band gaps. The use of the term "fully relativistic" is inherited from the terminology associated with pseudopotentials used in such DFT calculations [37] which indeed use the Dirac equation for the core atomic states—we do not use four-component Dirac-Kohn-Sham [38,39] DFT in this work. Likewise, calculations that begin with pseudopotentials that ignore spin-orbit coupling, but do include the relativistic mass correction and Darwin terms are called "scalar relativistic."

For materials with weak spin-orbit coupling, quasiparticle band structures incorporating spin-orbit coupling can be computed by separately calculating the additional contribution to the energy eigenvalues from spin-orbit coupling via conventional perturbation theory. First, wave functions $|n\mathbf{k}\rangle_0$ and energies $E^{\mathrm{QP}}_{n\mathbf{k},0}$ are computed from Dyson's Equation while neglecting spin-orbit coupling [30,31]:

$$\left[-\frac{\hbar^2\nabla^2}{2m_e} + V_{\mathrm{ion}} + V_{\mathrm{H}} + \Sigma\left(E^{\mathrm{QP}}_{n\mathbf{k},0}\right)\right]|n\mathbf{k}\rangle_0 = E^{\mathrm{QP}}_{n\mathbf{k},0}|n\mathbf{k}\rangle_0. \quad (2)$$

Corrections to the quasiparticle energies to include SOC are computed from diagonalizing the Hamiltonian [40,41]

$$H_{n_1,\mathbf{k},\alpha;n_2,\mathbf{k},\beta} = \langle n_1\mathbf{k}|_0 \langle\alpha| E^{\mathrm{QP}}_{n_1\mathbf{k},0}\delta_{n_1n_2}\delta_{\alpha\beta} + H^{\mathrm{SOC}}_{\alpha\beta}|\beta\rangle |n_2\mathbf{k}\rangle_0, \quad (3)$$

where $E^{\mathrm{QP}}_{n\mathbf{k}}$ is the quasiparticle energy for band n at k point $\mathbf{k}$, $H^{\mathrm{SOC}}_{\alpha\beta}$ is the spin-orbit coupling Hamiltonian, terms with the subscript "0" denote quantities that neglect spin, and $|\alpha\rangle$ and $|\beta\rangle$ are spinor basis states, $|\uparrow\rangle = (1, \quad 0)^T$ or $|\downarrow\rangle = (0, \quad 1)^T$. This approach, "$GW$+SOC," has been successfully used in *ab initio* calculations of diamond- and zinc-blende-structure semiconductors [42], metals such as Au [43], and topological insulators Bi_2Se_3 [44] and Bi_2Te_3 [45], among other systems. When the Kohn-Sham band structure neglecting spin-orbit coupling is qualitatively similar to the quasiparticle band structure that includes it, the GW+SOC approach is generally sufficient. Despite the success of perturbation theory in computing the changes of eigenvalues for materials with weak spin-orbit coupling, there is a clear need for a nonperturbative first-principles treatment of materials with strong spin-orbit coupling. In particular, some materials containing heavy elements, such as Bi_2Se_3 [46] and β-HgS [47,48], have DFT band structures that change significantly when spin-orbit coupling is included. In cases such as these, the perturbative GW+SOC approach is quantitatively or even qualitatively inaccurate.

Due to the doubled number of bands and doubled size of the wave functions compared to spinless calculations, there is a significant increase in the already substantial computational expense of many-body perturbation theory calculations, not to mention a significant increase in the complexity of the computer code. As a result, two-component spinor calculations with GW have only recently become available, and used in the literature. The all-electron FLAPW code SPEX's implementation [49] was later followed by pseudopotential and PAW codes (WEST [50], YAMBO [51], FHIAIMS [52], GPAW [53], and VASP [54]). There are yet fewer spinor BSE codes available; to date, only YAMBO [55] and BerkeleyGW have the capability to solve the Bethe-Salpeter equation with two-component spinor wave functions. While plane-wave DFT codes have become highly comparable in recent years due to increasing consensus on the best algorithms to use, and great efforts to determine the source of any discrepancies [56], there is a significant variation in the approaches used in GW/BSE codes, including not only basis sets and pseudopotentials, but also plasmon pole models, frequency integration, interpolation schemes, handling of the dielectric matrix, acceleration of sums over empty states, solution of Dyson's equation, and other numerical tricks and details. Such details are only sometimes spelled out comprehensively for a given code [57]. Benchmarking projects for GW codes—and especially for BSE—are still in their infancy. A notable example is the GW100 project which studied a set of molecules with different codes, each of which had its own distinct approaches to the GW problem [58].

We have implemented the spinor GW/BSE approach in BerkeleyGW in order to provide an independent implementation of this method for the general improvement of methodology in this area. This work also allows calculations in BerkeleyGW which is a widely used and well established code in the community, with extensive testing. BerkeleyGW also has particular advantages for GW/BSE with respect to massively parallel performance [59], Coulomb truncation and interpolation [57], and sampling schemes for reduced-dimensional systems [60]. In this paper, we present the results of this long-running implementation effort [61], with a detailed exposition of the formalism and in particular the handling of the effect of symmetries on spinors, which has not been explicitly addressed in previous literature on spinor GW/BSE. We also make careful comparisons to other codes, with their somewhat different technical details, to establish the level of agreement achieved among spinor GW calculations, and demonstrate the performance of spinor GW versus "scalar-relativistic" ("SR") GW calculations, in which only relativistic mass and Darwin terms are included in the construction of pseudopotentials, with SOC then included perturbatively. While we make several direct comparisons for quasiparticle energy gaps and spin-orbit splittings for

various conventional test systems such as group IV and III–V semiconductors with BerkeleyGW and other two-component spinor *GW* codes, the best comparison that is available for two-component spinor *GW*/BSE calculations for GaAs and GaSb is with empirical pseudopotential method calculations incorporating spin-orbit coupling perturbatively [62].

The ability to use two-component spinors in *GW* and *GW*/BSE scientific software allows for the study of magnetic phenomena in materials, beyond the usual single-axis spin-polarized calculations of self-energy corrections for majority and minority spin channels in materials such as bulk Fe and NiO_2 [63–66]. While spin susceptibilities have been approximated within the usual spin-polarized *GW* method [67–69], Ref. [70] derives results from many-body perturbation theory for susceptibilities describing spin-spin and spin-charge interactions. Spin susceptibilities [71] may then be used to calculate electron-magnon contributions to quasiparticle energies, as in the recent work in Ref. [72]. Other codes do not seem to have this functionality implemented. To assist in noncollinear or antiferromagnetic calculations, magnetic symmetry groups have been exploited in the code YAMBO to reduce the necessary size of magnetic systems to the primitive chemical unit cell [73]. While BerkeleyGW can treat magnetic systems within the supercell approach, the inclusion of spin susceptibilities, as well as the use of magnetic symmetry groups, is an ongoing work. We consider test systems with no magnetization in the present work.

This paper is structured as follows. In Sec. II, we review the theory of one-particle and two-particle excited states within many-body perturbation theory in the *GW* approximation, and how such calculations are performed in a plane-wave basis with wave functions that have two spinor components, and we discuss the appropriate treatment of crystal symmetries with spinorial wave functions, via quaternions, in a plane-wave basis set. In Sec. III, we demonstrate the accuracy of our implementation in the BerkeleyGW software package with calculations of the quasiparticle band structures and absorption spectra of materials containing small, moderate, and large spin-orbit coupling strength, where spin-orbit band splittings in conventional solids (all but Bi_2Se_3 in this work) are found to be equal within tens of meV whether computed from DFT or *GW*, while band gaps are generally improved with respect to experimental values from FR-*GW* compared to the perturbative treatment of spin-orbit coupling, by 100–200 meV. In Sec. IV, we compare to available results from other spinor *GW* codes [49–54,74,75], finding agreement within 10 meV for energy gaps compared to results from other codes—with the exception of Bi_2Se_3, a difficult case needing a more sophisticated treatment. In Sec. V, we discuss the additional expense of computations that use spinor wave functions. In Sec. VI, we conclude and give an outlook for future development in spinor *GW*/BSE.

II. SPINOR WAVE FUNCTIONS IN MANY-BODY PERTURBATION THEORY

We begin by quickly summarizing the changes in quantities involved in the *GW*/BSE approach with spinor wave functions. The derivation of the basic framework of Hedin's equations and the Bethe-Salpeter equation is presented in Ref. [76]. Similar derivations in the literature include Ref. [70] for Hedin's equations, Ref. [36] for computing quasiparticle energies within *GW*, and Ref. [55] for the Bethe-Salpeter Equation. Derivations including magnetic perturbations, not considered in this work, are performed in Ref. [77].

To begin, a mean-field solution (typically from Kohn-Sham DFT) is computed with fully relativistic pseudopotentials [78], in which spin is not a quantum number of the state (as in a spin-polarized or collinear calculation) but rather another argument of the wave function alongside $\mathbf{r}$. The Kohn-Sham wave function $\phi^{\mathrm{KS}}_{n\mathbf{k}}(\mathbf{r}) = \sum_{\alpha=\uparrow,\downarrow} \phi^{\mathrm{KS}}_{n\mathbf{k}\alpha}(\mathbf{r})|\alpha\rangle$, with $|\phi^{\mathrm{KS}}_{n\mathbf{k}\uparrow}|^2 + |\phi^{\mathrm{KS}}_{n\mathbf{k}\downarrow}|^2 = 1$, has the Kohn-Sham eigenvalue $\epsilon^{\mathrm{KS}}_{n\mathbf{k}}$:

$$\sum_{\alpha,\beta} \int d\mathbf{r} \left(\phi^{\mathrm{KS}}_{n\mathbf{k}\alpha}(\mathbf{r})\right)^{\dagger} H^{\mathrm{KS}}_{\alpha,\beta}\, \phi^{\mathrm{KS}}_{n\mathbf{k}\beta}(\mathbf{r}) = \epsilon^{\mathrm{KS}}_{n\mathbf{k}}. \tag{4}$$

Then, the matrix elements (Eq. (9) in Ref. [57]) are required for the computation in a plane-wave basis set of the RPA polarizability [79,80], matrix elements of the self-energy operator, matrix elements of the BSE kernel, and matrix elements of the velocity operator. These matrix elements

$$M_{nn'}(\mathbf{k}, \mathbf{q}, \mathbf{G}) = \sum_{\alpha} \langle n, \mathbf{k}+\mathbf{q}, \alpha | e^{i(\mathbf{q}+\mathbf{G})\cdot\mathbf{r}} | n', \mathbf{k}, \alpha \rangle \tag{5}$$

may be computed for all $\mathbf{G}$ by multiplying the Fourier transforms of the wave functions, for a spin component α common to both wave functions; computing the inverse Fourier transform of this product [57,81]; and then summing over spin index:

$$M_{nn'}(\mathbf{k}, \mathbf{q}, \{\mathbf{G}\}) = \sum_{\alpha} \mathrm{FFT}^{-1}(\phi^{*}_{n\mathbf{k}+\mathbf{q}\alpha}(\mathbf{r})\phi_{n'\mathbf{k}\alpha}(\mathbf{r})). \tag{6}$$

Since the (nonmagnetic [82]) polarizability has its physical origin from density fluctuations arising from the spin-independent Coulomb interaction, the form of the polarizability is identical to the case in which spin-orbit is neglected, apart from the sums over the spin index in the computation of the matrix elements in Eq. (6), the doubled number of both valence and conduction wave functions within the summation over basis states, and any differences in eigenfunctions and eigenvalues. In many cases, these differences are sufficiently small such that one may calculate the polarizability using the Kohn-Sham eigenfunctions and eigenvalues from a scalar-relativistic DFT calculation [36,83]. However, in this work, we use the Kohn-Sham eigenfunctions and eigenvalues from fully relativistic DFT calculations ("FR-DFT").

To calculate the optical absorption spectrum, we may first try to evaluate the imaginary part of the macroscopic dielectric function within the independent-particle approximation. We may readily determine, using the usual expression [84,85], the imaginary part of the dielectricfunction to be

$$\varepsilon_2(\omega) = \frac{8\pi^2 e^2}{\omega^2} \sum_{vc\mathbf{k}} \left| \boldsymbol{\lambda} \cdot \sum_{\alpha\beta} \langle v, \mathbf{k}, \alpha | \mathbf{v}_{\alpha\beta} | c, \mathbf{k}, \beta \rangle \right|^2 \times \delta(\omega - (E_{c\mathbf{k}} - E_{v\mathbf{k}})),$$

where $\boldsymbol{\lambda}$ is the direction of light polarization. The velocity operator $\mathbf{v} = i[H, \mathbf{r}]$ now has a spin-dependence inherited from the Hamiltonian. However, it can be transformed just as in the spin-independent case (explained in Ref. [57], containing

TABLE I. The kinetic energy cutoffs E_{cut}, calculated lattice parameters, experimental lattice parameters, Brillouin zone sampling, screened Coulomb cutoff ϵ_{cut}, and number of empty states used in the sums for both the polarizability ("Chi") and the Coulomb-hole ("COH") term in the self-energy. The pseudopotentials for Ge, Sb, Cd, and Au contain the full shell of the semicore states (e.g., $4s^2 4p^6 4d^{10}$ for Sb) [99]. The experimental lattice parameters are from Ref. [95]. For Si, Ge, GaP, GaAs, and GaSb, we use the same parameters as Ref. [42], and for Au, Ref. [106]. GaP results are discussed in Sec. IV.

	E_{cut} (Ry)	a_0^{relaxed}(Å)	$a_0^{\text{exp.}}$(Å)	**k** grid	ϵ_{cut} (Ry)	Empty states
Si	120	5.48	5.47	$8 \times 8 \times 8$	20	800
Ge	120	5.63	5.66	$8 \times 8 \times 8$	25	600 Chi, 1000 COH
GaP	350	5.45	5.45	$8 \times 8 \times 8$	40	800 Chi, 1000 COH
GaAs	350	5.61	5.65	$8 \times 8 \times 8$	20	1002
GaSb	350	6.09	6.10	$8 \times 8 \times 8$	20	1002
CdSe	200	4.30	4.30	$6 \times 6 \times 4$	20	996
Au	72	4.08	4.08	$8 \times 8 \times 8$	50	2018

a few additional details or corrections compared to Ref. [57]) into

$$\langle v, \mathbf{k}|\mathbf{v}|c, \mathbf{k}\rangle = -i(E_{c\mathbf{k}} - E_{v\mathbf{k}})\langle v, \mathbf{k}|\mathbf{r}|c, \mathbf{k}\rangle \tag{7}$$

containing now a spin-independent dipole operator. We evaluate in practice:

$$\varepsilon_2(\omega) = 8\pi^2 e^2 \sum_{vc\mathbf{k}} \left| \boldsymbol{\lambda} \cdot \sum_{\alpha} \langle v, \mathbf{k}, \alpha|\mathbf{r}|c, \mathbf{k}, \alpha\rangle \right|^2 \times \delta(\omega - (E_{c\mathbf{k}} - E_{v\mathbf{k}})),$$

where the dipole matrix element is calculated via a $\mathbf{q} \to 0$ limit. The momentum operator $-i\nabla$ can be used to approximate $\mathbf{v}$ to avoid needing a set of wave functions on a shifted k grid, but this is a worse approximation than in the spinless case, as the fully relativistic Hamiltonian contains additional nonlocal terms, not only the spin-orbit coupling but also both of the scalar relativistic terms [86].

When we use the BSE with interacting two-component spinor electron and hole wave functions, the absorption spectrum is then computed from

$$\epsilon_2(\omega) = 8\pi^2 e^2 \sum_{S} \left| \sum_{vc\mathbf{k}} A^S_{vc\mathbf{k}} \boldsymbol{\lambda} \cdot \sum_{\alpha} \langle \mathbf{k}, \alpha|\mathbf{r}|c, \mathbf{k}, \alpha\rangle \right|^2 \times \delta\left(\omega - \Omega^S\right),$$

using the excitonic version of Eq. (7) [57]. We take the Tamm-Dancoff approximation ("TDA") for the BSE Hamiltonian [87] in this equation for the imaginary part of the dielectric function, though some systems require consideration of the full BSE Hamiltonian [88]. Calculations beyond the TDA for BSE with BerkeleyGW [89] are also compatible with spinor wave functions, though this feature is not considered in this work.

TABLE II. The values of the Brillouin zone sampling of the fine grid, the number of valence and conduction bands used as the basis for the BSE, and the Gaussian broadening of the delta function.

	$\mathbf{k}_{\text{fine}}$ grid	N_v	N_c	Broadening (meV)
GaAs	$12 \times 12 \times 12$	6	8	150
GaSb	$12 \times 12 \times 12$	6	8	100
Au	$12 \times 12 \times 12$	6	4	150

We also note that in the presence of spin-orbit coupling, spin is generally no longer a good quantum number, so it is no longer possible to refactor the Bethe-Salpeter Hamiltonian into spin-singlet and -triplet block-diagonal submatrices [32]. Further, the number of valence and conduction bands both double, relative to spinless calculations. This makes explicit diagonalization of the BSE Hamiltonian, which scales as $N^3_{\text{basis}} = (N_v N_c)^3$, more expensive by a factor of 64 for solids, as the basis has quadrupled. However, the time spent performing this diagonalization and computation of the absorption spectraremains a relatively rapid calculation, compared to calculation of the screened interaction and the self-energy (see Sec. V).

The most formidable computational challenge with the inclusion of two-component spinor wave functions is the increase in the number of charge-density matrix elements [Eq. (6), which must be calculated for the polarizability, self-energy, and BSE kernel]. Compared to a calculation performed on the same system without spin, the number of both valence and conduction states double. Taking the ratio of the scaling of the charge-density matrix element calculation with system size N [57], we find an increase in computation time by

$$\frac{(2N)^2\, 2\ln(2N)}{N^2 \ln N} = 8(1 + \log_N 2), \tag{8}$$

where the additional factor of 2 in the numerator comes from having to compute the inverse-FFT for each of the of two-component spinor wave functions. Since, at best, we are increasing the cost of matrix element calculations by more than a factor of 8, we should make use of symmetries of the Brillouin zone to allow for converged calculations within reasonable computational cost. (Detailed discussion about the performance of the major sections of the BerkeleyGW code is included in Sec. V.)

1. Symmetries, with spinor wave functions

Finally, we summarize results regarding the use of symmetries with spinor wave functions, since BerkeleyGW constructs Kohn-Sham wave functions in the full Brillouin

TABLE III. The band gap and spin-orbit splitting for Si, computed at the FR-LDA and FR-*GW* levels, compared to experiment. The fundamental band gap from experiment is reported with zero-point renormalization corrections.

	FR-LDA	FR-*GW*	*GW*+SOC [42]	Experiment
E_g (eV)	0.45	1.22	1.27	1.22 [114], 1.23 [115]
$E(\Gamma_{6c}) - E(\Gamma_{8v})$ (eV)	2.46	3.22	3.28	3.34 [116]
$\Delta^{\mathrm{SOC}}(\Gamma, v)$ (eV)	0.05	0.05	0.05	0.044 [95]
$\Delta^{\mathrm{SOC}}(\Gamma, c)$ (eV)	0.03	0.04	0.04	0.030–0.040 [95]
$\Delta^{\mathrm{SOC}}(L, v)$ (eV)	0.03	0.03	0.03	0.030 [95]
$\Delta^{\mathrm{SOC}}(L, c)$ (eV)	0.01	0.01	0.02	–

zone from those calculated in an irreducible wedge [57]. More details are included in Ref. [76].

Spinor Bloch functions are written

$$\psi_{n\mathbf{k}}(\mathbf{r}) = u_{n\mathbf{k}\uparrow}(\mathbf{r})e^{i\mathbf{k}\cdot\mathbf{r}}\chi_\uparrow + u_{n\mathbf{k}\downarrow}(\mathbf{r})e^{i\mathbf{k}\cdot\mathbf{r}}\chi_\downarrow \tag{9}$$

and χ_α represents a spinor. The periodic functions $u_{n\mathbf{k}\uparrow}$ and $u_{n\mathbf{k}\downarrow}$ are spatial and thus transform according to the usual treatment of symmetries. However, the spinor itself rotates according to the rules oftransformation for elements of the group SU(2):

$$\begin{aligned} P_{\{\mathrm{R}|\boldsymbol{\tau}\}}\psi_{n\mathbf{k}}(\mathbf{r}) = {} & \tilde{u}_{n\mathrm{R}\mathbf{k}\uparrow}(\mathbf{r})\exp(i\mathrm{R}\mathbf{k}\cdot\mathbf{r})\exp(i\,\hat{n}\cdot\vec{\sigma}\,\theta/2)\chi_\uparrow \\ & + \tilde{u}_{n\mathrm{R}\mathbf{k}\downarrow}(\mathbf{r})\exp(i\mathrm{R}\mathbf{k}\cdot\mathbf{r})\exp(-i\,\hat{n}\cdot\vec{\sigma}\,\theta/2)\chi_\downarrow, \end{aligned} \tag{10}$$

where $\hat{n}$ and θ are the unit-axis and angle (about the axis $\hat{n}$) that recreates the rotational action of the symmetry operation R.

By calculating from the rotation matrix R a quaternion q that is guaranteed to be nonsingular [90–92], we evaluate the rotation angle θ from

$$\theta = 2\arctan\left(\frac{q_1^2+q_2^2+q_3^2}{q_4}\right), \tag{11}$$

where arctan is a function with all real numbers as its domain, and evaluate the i'th component of the axis of rotation n_i from

$$n_i = \frac{q_i}{\sqrt{q_1^2+q_2^2+q_3^2}}. \tag{12}$$

The set of rotation matrices R for a crystalline system are usually stored in the basis of lattice vectors in *ab initio* codes, as it allows these matrices (up to 48 in number) to be written with nine integers. In this case, we must transform the rotation matrices in the lattice basis, $\mathrm{R}^{\mathrm{lat}}$, to the rotation matrix in the Cartesian basis. If we form a matrix A out of the lattice vectors, this transformation is

$$\mathrm{R}^{\mathrm{cart}} = A\mathrm{R}^{\mathrm{lat}}A^{-1}. \tag{13}$$

If instead we decide to use the reciprocal lattice vectors $\mathbf{b}_1$, $\mathbf{b}_2$, $\mathbf{b}_3$ to construct the matrix B in a fashion as in the above, we make use of the identity $B^{\mathrm{T}}A = 2\pi I$ to write

$$\mathrm{R}^{\mathrm{cart}} = (B^{\mathrm{T}})^{-1}\mathrm{R}^{\mathrm{lat}}B^{\mathrm{T}}. \tag{14}$$

This latter choice is beneficial if the matrices A and B are in fact stored as their transposes, as some codes do.

Finally, we note that in the presence of inversion symmetries, "improper rotations" S must be considered. While improper rotations are often considered to be the composition of a rotation and a mirror reflection about the plane perpendicular to the axis of the rotation, instead we can consider the improper rotation S to be (in general, a different) rotation R followed by inversion N, $S = N\mathrm{R}$ [93]. However, if both spatial inversion and time-reversal operations commute with the Hamiltonian under consideration, the (spinor) wave function is a simultaneous eigenstate of both symmetries. Thus in the presence of only time-reversal symmetric terms in the Hamiltonian, the wave functions are unaffected by inversion, apart from perhaps an overall phase factor. We identify improper rotations by the property $\det(S) = -1$, and if detected, use only the rotation part R of S to transform the spinor components of the wave function.

TABLE IV. The band gap and spin-orbit splittings for Ge, computed at the FR-LDA and FR-*GW* levels, compared to experiment. Experimental data are from Ref. [95] unless otherwise specified.

	FR-LDA	FR-*GW*	*GW*+SOC [42]	Experiment
E_g (eV)	0.13	0.74	0.54	0.79
$E(\Gamma_{7c}) - E(\Gamma_{8v})$ (eV)	0.15	0.96	0.38	0.90
$\Delta^{\mathrm{SOC}}(\Gamma, v)$ (eV)	0.31	0.30	0.32	0.297
$\Delta^{\mathrm{SOC}}(\Gamma, c)$ (eV)	0.22	0.21	0.24	0.200
$\Delta^{\mathrm{SOC}}(L, v)$ (eV)	0.19	0.19	0.20	0.228
$\Delta^{\mathrm{SOC}}(L, c)$ (eV)	0.10	0.08	0.12	–

III. TEST SYSTEMS

We present results for seven different materials with a wide range of spin-orbit coupling (SOC) strengths. The diamond and zincblende semiconductors Si, Ge, and GaAs are technologically important materials with weak SOC. GaSb has a spin-orbit splitting of its valence bands of similar magnitude as its band gap. CdSe has a wurtzite structure and a significant SOC (429 meV [94], over 25 times larger than that of wurtzite GaN, 16.8 meV [95]). Au is a prototypical metal with strong SOC. Finally, Bi_2Se_3 has a nontrivial topological nature due to the bandinversion induced by its strong SOC, and is a particularly challenging case to explore which has been studied in much previous literature.

A. Computational details

We compute mean-field wave functions and eigenvalues from density functional theory [28,29]. For the exchange-correlation energy, we employ the Perdew-Zunger

TABLE V. The band gap and spin-orbit splitting for GaAs, computed at the FR-LDA and FR-*GW* levels, compared to experiment. Experimental data are from Ref. [95] unless otherwise specified.

	FR-LDA	FR-*GW*	*GW*+SOC [42]	Experiment
E_g (eV)	0.55	1.49	1.31	1.57 [117]
$\Delta^{\mathrm{SOC}}(\Gamma, v)$ (eV)	0.32	0.34	0.35	0.340
$\Delta^{\mathrm{SOC}}(\Gamma, c)$ (eV)	0.19	0.17	0.20	0.171
$\Delta^{\mathrm{SOC}}(L, v)$ (eV)	0.20	0.21	0.22	0.22
$\Delta^{\mathrm{SOC}}(L, c)$ (eV)	0.08	0.07	0.09	0.05

TABLE VI. The band gap and spin-orbit splittings for GaSb, computed at the FR-LDA and FR-*GW* levels, compared to experiment. Experimental data are from Ref. [95].

	FR-LDA	FR-*GW*	*GW*+SOC [42]	Experiment
$E(\Gamma_{6c}) - E(\Gamma_{8v})$ (eV)	0.14	0.82	0.70	0.822
$E(L_{6c}) - E(\Gamma_{8v})$ (eV)	0.25	0.78	0.85	0.907
$\Delta^{\mathrm{SOC}}(\Gamma, v)$ (eV)	0.74	0.73	0.73	0.756
$\Delta^{\mathrm{SOC}}(\Gamma, c)$ (eV)	0.23	0.20	0.21	0.213
$\Delta^{\mathrm{SOC}}(L, v)$ (eV)	0.42	0.42	0.42	0.430
$\Delta^{\mathrm{SOC}}(L, c)$ (eV)	0.12	0.09	0.12	0.13

parametrization of the LDA [96]. We generate fully relativistic pseudopotentials using the optimized norm-conserving Vanderbilt pseudopotential (ONCVPSP) scheme [97] with parameters from the pseudo-Dojo pseudopotential database [98]. The pseudopotentials for Au, Bi, Cd, Ga, Ge, and Sb contain the full shell of the semicore states (e.g., $5s^2 5p^6 5d^{10}$ for Bi) for accurate calculation of the bare exchange [99]. All DFT calculations are carried out with the QUANTUM ESPRESSO software package [100].

We first determine the equilibrium lattice constants and atom positions. Table I shows that all relaxed lattice constants are in very good agreement with experimental measurements. We instead use the experimental lattice parameters and atomic coordinates for Bi_2Se_3 due to the sensitivity of its DFT band structure with respect to its geometry [101].

Next, the quasiparticle energies are computed with the one-shot "G_0W_0" approach, using the Hybertsen-Louie generalized plasmon pole model [31,102] for the inverse dielectric matrix. For the case of bulk Au, we also calculated the quasiparticle band structure in the Godby-Needs plasmon pole model [103] and found differences of 50 meV or smaller in the quasiparticle energies, in the range 6 eV above and below the Fermi energy [76]. For the test systems Si, Ge, and GaAs, the difference in computed band gaps when using the Hybertsen-Louie and Godby-Needs plasmon pole models is tens of meV [104], and the difference between the Godby-Needs plasmon pole model and the Hybertsen-Louie plasmon pole model results for the band gap of Bi_2Se_3 is presumed to be similar in magnitude to the difference between the Hybertsen-Louie GPP and full-frequency results, also tens of meV. The difference in computed band gaps can be an order of magnitude larger for systems with localized electrons such as transition metal oxides [104].

Table I summarizes our parameters for the empty state summations, the k-point sampling, and the plane-wave cutoffs for the dielectric matrices. We use the static remainder method to improve convergence with the number of empty states in the Coulomb-hole summation [105]. We verified that G_0W_0 evaluation of the self energy in the band-diagonal approximation yields quantitatively accurate band structures for these test systems. Deviations from this methodology in the computation of the band structure for Bi_2Se_3 are enumerated in Sec. III D.

The k-point sampling and number of bands used in constructing the *GW*/BSE Hamiltonian are summarized in Table II. All excited-state calculations are carried out with the BerkeleyGW software package.

B. Summary of band structure for Si, Ge, GaAs, GaSb, CdSe, and Au

Since the band structures for Si, Ge, GaAs, GaSb, CdSe, and Au are well-known and differ little when either including or disregarding spin-orbit coupling, we briefly summarize the different approaches to their calculation and the results. Figures for these band structures are included in Ref. [76].

In Tables III, IV, V, and VI we compare values of interband gaps labeled according to irreducible representation, with c for conduction band and v for valence band, as well as spin-orbit split bands, labeled by high-symmetry point in the Brillouin zone, for the valence and conduction bands nearest in energy to the band gap that exhibit spin-orbit splitting. We compare values as computed from FR-LDA, FR-*GW*, and *GW*+SOC, with the latter from Ref. [42], along with experimental values.

These diamond/zincblende semiconductors with small to moderate spin-orbit coupling have spin-orbit splitting values that are consistent within few tens of meV or better, regardless of the calculation method. The band gaps are of course underestimated within FR-LDA, while FR-*GW* and *GW*+SOC values differ by as much as 0.2 eV for all but Si. In the case of Ge, we attribute the underestimated band gaps from Ref. [42] from the use of a Ge pseudopotential that freezes the $n = 3$ semicore states in the core, rather than to inherent limitations of the perturbative approach.

Additionally, these standard Group IV or III–V semiconductors may have their band gaps estimated by an approach that combines more easily computed quantities, the band gap $E_g^{\text{SR-}GW}$ from SR-*GW* and the valence band spin-orbit splitting $\Delta^{\mathrm{SOC}}_{\mathrm{LDA}}(\Gamma, v)$ from FR-LDA. The valence-band maximum is taken to be purely atomic (cationic, for compound semiconductors) p states, which split due to spin-orbit coupling as in a free atom, with $p_{3/2}$ states shifting upward in energy by $\frac{1}{3}\Delta^{\mathrm{SOC}}$ and $p_{1/2}$ downward by $\frac{2}{3}\Delta^{\mathrm{SOC}}$ [107]. Within this "atomic perturbation theory" approach,

$$E_g^{GW+\mathrm{SOC}} \approx E_g^{\text{SR-}GW} - \tfrac{1}{3}\Delta^{\mathrm{SOC}}_{\mathrm{LDA}}(\Gamma, v). \tag{15}$$

The "atomic SOC perturbation" estimates for the band gaps of Ge (0.95 eV), GaAs (1.49 eV), and GaSb (0.82 eV) agree with the FR-*GW* values within 10 meV.

Wurtzite CdSe has fewer comparable calculations in the literature, so we report the FR-LDA and FR-*GW* values computed for the band gap, spin orbit splitting of the valence band maximum, and the crystal field splitting of the Γ_6 and

TABLE VII. The band gap and spin-orbit splitting for CdSe, computed at the FR-LDA and FR-*GW* levels, compared to experiment. The spin-orbit (SOC) and crystal field (CF) splitting refers to the states at the top of the valence band at Γ. Experimental data are from Ref. [94].

	FR-LDA	FR-*GW*	Experiment
E_g (eV)	0.58	1.85	1.84
$\Delta^{\mathrm{SOC}}(\Gamma, v)$ (eV)	0.372	0.405	0.429
$\Delta^{\mathrm{CF}}(\Gamma, v)$ (eV)	0.036	0.026	0.026

Γ_1 valence bands in Table VII. FR-GW values agree with experimental values within a few meV.

For Au, Table VIII shows that the quasiparticle energies are generally improved with FR-*GW* compared to FR-LDA, especially near the Fermi level. The FR-*GW* quasiparticle energies are in good agreement with a quasiparticle self-consistent *GW* ("QS*GW*") calculation in which SOC is added perturbatively, from Ref. [43], indicating that the perturbative treatment of SOC for the band structure is sufficient. The Fermi level for FR-*GW* and SR-*GW* is recalculated using the the Blöchl tetrahedron method [108] with the quasiparticle energies, from the CMS-PY PYTHON library [109]. The quasiparticle energies are largely similar whether using the Hybertsen-Louie or the Godby-Needs GPP model, within an energy range of 6 eV above or below the Fermi level [76].

C. Absorption spectra for GaAs, GaSb, and Au

For GaAs, the absorption spectrum differs little when computed from SR-*GW*/BSE or FR-*GW*/BSE, as the spin-orbit split "E_1" and "$E_1 + \Delta$" pair of peaks is split by 200 meV, which is on the order of the resolution of the calculation (150 meV) with the given fine-grid k-point sampling of $12 \times 12 \times 12$ and is thus obscured. The GaAs spectra is included in Ref. [76].

TABLE VIII. The FR-LDA and FR-*GW* band energies in eV for Au relative to the Fermi energy, as compared to QS*GW*+SOC and experiment. Bands at high-symmetry k points are labeled according to their double-group irreducible representation (see Ref. [43]).

	FR-LDA	FR-*GW*	QS*GW*+SOC [43]	Experiment
Γ_6^+	−10.17	−10.22	−10.39	−−
Γ_8^+	−5.69	−6.05	−6.02	−5.09[a], −6[b], −6.01[c]
Γ_7^+	−4.58	−4.89	−4.85	−4.45[a], −4.6[b], −4.68[c]
Γ_8^+	−3.29	−3.67	−3.67	−3.55[a], −3.65[b], −3.71[c]
Γ_7^-	13.91	14.46	15.36	16[c], 15.9[d]
Γ_6^-	17.26	17.81	17.97	18.8[c]
L_6^+	−7.84	−8.11	−8.01	−7.8[b]
$L_{4,5}^+$	−5.80	−6.21	−6.16	−6.23[b], −6.2[c]
L_6^+	−4.69	−5.08	−4.97	−4.88[b], −5[c]
L_6^+	−2.56	−2.87	−2.95	−3.2[c]
$L_{4,5}^+$	−1.90	−2.19	−2.24	−2.3[c], −2.5[e]
L_6^-	−1.32	−1.26	−1.63	−1[e], −1[f], −1.01[g], −1.1[h]
L_6^+	3.09	3.44	3.19	3.6[e], 3.65[f], 3.56[g], 3.4[h]

[a]Reference [119].
[b]Reference [120].
[c]Reference [121].
[d]Reference [122].
[e]Reference [123].
[f]Reference [124].
[g]Reference [125].
[h]Reference [126].

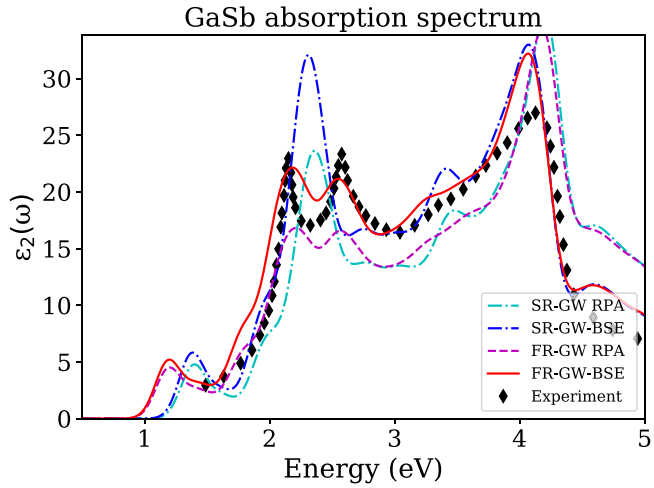

FIG. 1. The absorption spectra of GaSb, calculated at the SR-*GW*-RPA (cyan), SR-*GW*/BSE (blue), FR-*GW*-RPA (magenta), and FR-*GW*/BSE (red) levels. RPA spectra are included to assess any renormalization of SOC by the electron-hole interaction. Experimental results are from Ref. [110].

Figure 1 shows the absorption spectrum for GaSb calculated with the SR-*GW*/BSE and FR-*GW*/BSE methods, as well as the noninteracting "RPA" method, in which the electron-hole kernel in the Bethe-Salpeter Equation is disregarded, as well as a comparison with experiment [110]. The RPA spectra are included to assess any differences in the spin-orbit split peaks E_1 and $E_1 + \Delta$ due to renormalization of SOC from the electron-hole interaction.

The absorption spectrum of GaSb has significant differences when including SOC. First, the absorption onset is shifted by 190 meV due to the large difference in the quasiparticle band gap when including (0.82 eV) or neglecting SOC (1.07 eV). Also, we can clearly resolve the 2.3 eV peak splitting into the E_1 and $E_1 + \Delta$ peaks with the inclusion of SOC. The E_1 and $E_1 + \Delta$ peak placements at 2.18 and 2.54 eV agree well with the experimental [110] spectrum peak placements of 2.18 and 2.62 eV, respectively, and the EPM+SOC peak placements of 2.22 and 2.86 eV [62]. These results, as well as the energies of the E_0 and E_2 peaks, are included in Table IX. The absorption spectra computed within RPA are qualitatively similar to that of the BSE, with the E_1

TABLE IX. Absorption peak energies for GaSb, in eV. The $E_0 + \Delta$ does not appear in Ref. [62] or Ref. [118].

	FR-*GW*/BSE	EPM+SOC [62]	Experiment [118]
$E_0 + \Delta$	1.19	–	–
E_1	2.18	2.22	2.184
$E_1 + \Delta$	2.54	2.86	2.618
E_2	4.06	4.37	4.286

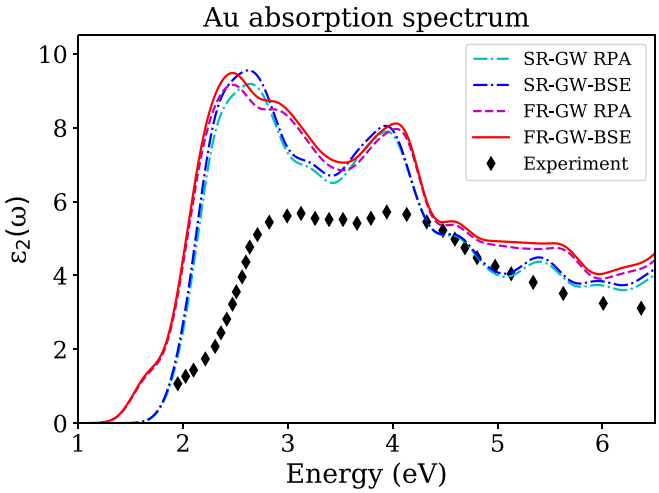

FIG. 2. The absorption spectrum of Au due to interband transitions, calculated at the *GW*/BSE level. Spin orbit is included (neglected) in the red (blue) curve. The experimental spectrum is from Ref. [112].

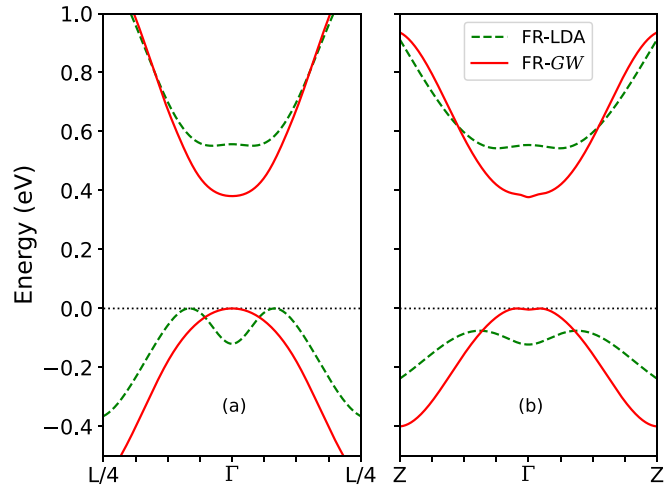

FIG. 3. The electronic band structure of Bi_2Se_3 along the (a) Γ to *L* and (b) Γ to *Z* directions, including spin-orbit coupling, but only Hamiltonian matrix elements that are diagonal at the FR-*GW* level: fully relativistic ("FR") LDA and *GW* in dashed green and solid red lines, respectively.

and $E_1 + \Delta$ peak splitting agreeing with that of the BSE under 10 meV, indicating no significant renormalization effects of SOC from the electron-hole interaction.

The calculated interband absorption spectrum for Au shown in Fig. 2 shows a redshift in the onset of absorption with the inclusion of spin-orbit coupling, and an additional absorption peak at 1.6 eV, with the absorption spectra having minor qualitative changes when including the electron-hole interaction ("BSE") or not ("RPA"). The optical properties of Au are well-known to be impacted by relativistic effects [111], and the inclusion of only scalar relativistic effects is insufficient for a description of its absorption of visible light [111]. The redshift of the absorption onset compared to the experimental data from Ref. [112] is understood from the LDA starting point leading to an underestimation of the energy relative to the Fermi level for the lowest-energy unoccupied band at the *X* point. The use of orbital-dependent functionals in DFT ameliorates this underestimation [113], and presumably some level of self-consistency in *GW* beyond one-shot G_0W_0 would also correct the underestimation. The absorption spectrum was calculated with a $12 \times 12 \times 12$ *k*-point sampling, six valence bands, and four conduction bands.

D. Bi_2Se_3

While the previous test systems confirm the sufficiency of treating SOC as a perturbation, the *GW*+SOC approach for the band structure of Bi_2Se_3 has shown mixed results [44,83]. The large spin-orbit splitting of the Bi $6p$ electrons inverts the positive and negative parity *p*-like states (from the Bi $6p$ and Se $4p$ orbitals) near the band gap, creating a nontrivial value of the Z_2 topological index [46]. The "inverted" band gap is caused by the level repulsion of the inverted states at the Γ point, mixing the character of the conduction and valence states within a neighborhood of Γ [44]. The strength of this level repulsion depends on the size of the band gap, which is underestimated in DFT. As a consequence, the band structure computed from DFT and *GW* differ significantly when SOC is included, so the perturbative treatment may be insufficient.

Due to the sensitivity of this system to the DFT functional and the atomic geometry [101], in our study of the bulk band gap of Bi_2Se_3 as computed within FR-*GW*, we use the experimental geometry [95]. For consistency with the majority of previous calculations in the literature [44,83,127,128], we use the LDA functional. We use a Brillouin zone sampling of $8 \times 8 \times 8$ for constructing the charge density as well as the dielectric function. We use a 160 Ry cutoff for the plane-wave basis for the wave functions and a 25 Ry cutoff for the dielectric function. The polarizability ("Chi") summation uses 1000 unoccupied bands, and the Coulomb-hole ("COH") summation uses 1254 bands. The quasiparticle energies are estimated to be converged within about 30 meV [76].

We obtain the band structure in the neighborhood of the Γ point by obtaining quasiparticle energies at the Γ point and at particular points along the Γ-to-*L* and the Γ-to-*Z* high-symmetry lines, shown in Fig. 3. Ordinarily, band structures are determined from the set of quasiparticle energies computed on coarse, regularly spaced *k*-point grid and a set of overlap coefficients computed for the wave functions on the coarse grid and DFT-computed wave functions that densely sample high-symmetry lines in the Brillouin zone [57]. This approach does not work well, however, in cases such as Bi_2Se_3, especially near the Γ point where the DFT band structure and the quasiparticle band structure disagree significantly. Instead, we directly compute quasiparticle energies along the Γ-to-*L* direction at $\frac{1}{16}L$, $\frac{1}{8}L$, $\frac{3}{16}L$, and $\frac{1}{4}L$, and along the Γ-to-*Z* direction at $\frac{1}{16}Z$, $\frac{1}{8}Z$, $\frac{3}{16}Z$, $\frac{1}{4}Z$, $\frac{1}{2}Z$, and *Z*. The whole Γ-to-*Z* line is represented as it is a much shorter path in the Brillouin zone than the Γ-to-*L* line. We then plot spline-interpolated curves as estimates to the quasiparticle band structure. The LDA band structure interpolated in a similar fashion shows good agreement with the band structure calculated explicitly at each *k* point [76]. The (band-diagonal) FR-*GW* band struc-

ture along the Γ-to-Z line suggests that the band-diagonal approximation is not generally sufficient, as is apparent from the appearance of small, spurious [83,127,129] bumps in both the conduction and valence bands in a very narrow region about Γ (Fig. 3). These bumps are also seen in Ref. [130] for Bi_2Te_3 in the F-Γ-L k-point path, but are small along that path for both Bi_2Se_3 and Sb_2Te_3.

We find a direct bulk band gap of 0.38 eV in the band-diagonal approximation, which is in good agreement with values obtained from angle-resolved photoemission spectroscopy (ARPES) [127] (0.332 eV) as well as scanning tunneling spectroscopy (STS) [131] (0.3 eV). Optical measurements of the gap, however, report a smaller value of 0.2 eV [129] and also confirm a direct band gap at Γ.

To improve the quasiparticle band structure, we investigate the effect of including band-off-diagonals in the calculation of the self-energy matrix elements:

$$E_{n\mathbf{k}} = \mathrm{Eig}(\epsilon_{l\mathbf{k}}\delta_{lm} + \langle l, \mathbf{k}, \alpha|\Sigma_{\alpha\beta}(E_{p\mathbf{k}}) - V^{\mathrm{xc}}\delta_{\alpha\beta}|m, \mathbf{k}, \beta\rangle), \tag{16}$$

where "Eig" denotes the eigenvalues of the matrix constructed from the self-energy in the Kohn-Sham orbital basis, the band n is a member of the set of wave functions spanned by all choices for the indices l and m, and the energy $E_{p\mathbf{k}}$ at which the self-energy operator is evaluated is chosen from either the row ($E_{l\mathbf{k}}$) or column ($E_{m\mathbf{k}}$), as the difference in eigenvalues from this choice and an explicitly constructed Hermitian matrix for the self-energy correction,

$$\tfrac{1}{2}(\langle l, \mathbf{k}, \alpha|\Sigma_{\alpha\beta}(E_{l\mathbf{k}}) - V^{\mathrm{xc}}\delta_{\alpha\beta}|m, \mathbf{k}, \beta\rangle + \langle l, \mathbf{k}, \alpha|\Sigma_{\alpha\beta}(E_{m\mathbf{k}}) - V^{\mathrm{xc}}\delta_{\alpha\beta}|m, \mathbf{k}, \beta\rangle), \tag{17}$$

as used for quasiparticle self-consistent *GW* [132,133] (QS*GW*), is found to be under 1 meV. The QS*GW* approach involves reevaluating sums over empty states in both the dielectric screening and the self-energy to arrive at converged quasiparticle wave functions, whereas single diagonalization is a first correction to the "one-shot" G_0W_0, which supposes Kohn-Sham wave functions as close enough to the quasiparticle wave functions.

We find that the choice of the four valence wave functions and two conduction wave functions near the Fermi energy is sufficient to correct the deficiencies in the band structure when using the LDA eigenfunctions as the quasiparticle wave functions [76]. The band structure computed in this fashion is shown in Fig. 4. The band gap computed at first iteration is 0.33 eV, though we rigidly shift the gap to match that of the diagonal approximation, 0.38 eV, which is justified in the discussion after Eq. (20).

The necessity of calculating a matrix for the self-energy can be seen by noting that the strength of the level repulsion—and therefore the character of the wave functions – depends on the band gap value [44]. When changing the gap, as in a *GW* calculation, the wave functions in the region where the character is inverted necessarily change along with the extent of the region in the band structure with inverted orbital character. In Ref. [130], the authors analyze the atomic orbital contributions to bands featuring bumps when computing the band structure of Bi_2Te_3 and find that, for bands with avoided crossings due to spin-orbit coupling, these bands in

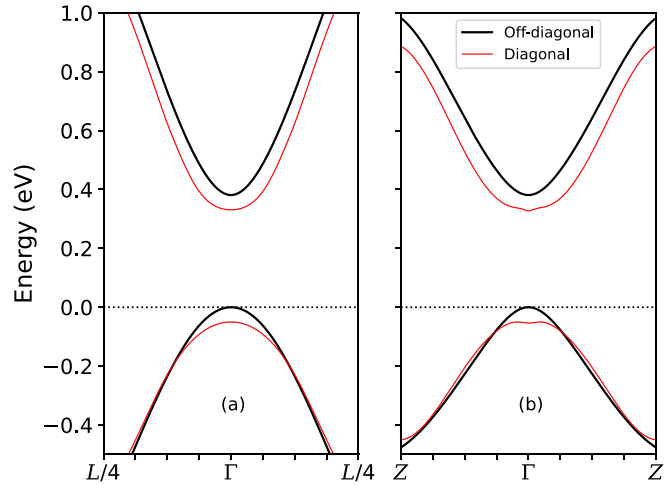

FIG. 4. The electronic band structure of Bi_2Se_3 along the (a) Γ to L and (b) Γ to Z directions, including spin-orbit coupling: the quasiparticle band structure computed from FR-*GW* with off-diagonal entries in the Hamiltonian (solid black), and the quasiparticle band structure without off-diagonals (solid, thinner red) and arbitrarily shifted downward by 0.05 eV for clarity.

the LDA basis have a very narrow region in which band inversion occurs, leading to sharp spikes. The updated off-diagonal basis however has a more extended region of band inversion, allowing for a smoother band structure, consistent with the update in the band gap from LDA to *GW*. The use of the LDA basis, then, is not adequate for an accurate band structure in this region, nor are self-consistent schemes such as eigenvalue self-consistent *GW* that do not update the quasiparticle basis set. QS*GW* would update the LDA basis, along with updating estimates of the screening and self-energy [132]. However, QSGW schemes that do not explicitly include vertex corrections beyond the usual *GW* approximation can often overestimate band gaps in solids by as much as 20% [134,135]. Instead, this first-iteration approach to update the basis set provides us an efficient means of correcting the basis set without having to carry through a full self-consistent cycle that would require an additional contribution from vertex corrections.

In the usual band-diagonal approximation to the self-energy operator two energies are calculated [57]. First, the self-energy operator is evaluated at the mean-field eigenvalues, giving the first of these energies:

$$E^0_{n\mathbf{k}} = \epsilon^{\mathrm{DFT}}_{n\mathbf{k}} + \langle n\mathbf{k}|\Sigma\left(\epsilon^{\mathrm{DFT}}_{n\mathbf{k}}\right) - V^{\mathrm{xc}}|n\mathbf{k}\rangle. \tag{18}$$

Σ is evaluated (within default settings in BerkeleyGW) at $\epsilon^{\mathrm{DFT}}_{n\mathbf{k}}$ and $\epsilon^{\mathrm{DFT}}_{n\mathbf{k}} + 1$ eV, from which the derivative $\frac{d\Sigma_{n\mathbf{k}}}{dE}$ and the renormalization factor

$$Z_{n\mathbf{k}} = \frac{1}{1 - \frac{d\Sigma_{n\mathbf{k}}}{dE}} \tag{19}$$

are computed. The quasiparticle energy $E^{\mathrm{QP}}_{n\mathbf{k}}$ can then be determined from Newton's method and written as

$$E^{\mathrm{QP}}_{n\mathbf{k}} = Z_{n\mathbf{k}}E^0_{n\mathbf{k}} + (1 - Z_{n\mathbf{k}})\epsilon^{\mathrm{DFT}}_{n\mathbf{k}}. \tag{20}$$

However, in band-of-fdiagonal calculations, the renormalization factors Z cannot be computed in this way and thus the

Newton's method approach to determining the quasiparticle energy cannot be performed. The self-energy operator is a function of energy, and a solution to Dyson's equation is found when this input energy is the same as the eigenvalue of the Hamiltonian in Eq. (16). Initially, the Kohn-Sham energy eigenvalues are used as input for the self-energy, and the basis set is taken to be the Kohn-Sham wave functions. After diagonalization, a new set of energy eigenvalues and wave functions (expressed as a linear combination of the Kohn-Sham wave functions) are used to construct a new Hamiltonian, which is then diagonalized. This process is repeated until the energy eigenvalues do not substantially change from one iteration step to another—only at that final iteration are the energy eigenvalues the quasiparticle energies.

After a first diagonalization of the Hamiltonian constructed with Kohn-Sham energies and bands, the difference between valence band maximum and conduction band minimum at the Γ point is 0.33 eV. This energy is analogous to the $E^0_{n\mathbf{k}}$ energies in Eq. (18). However, since all off-diagonal terms for the self-energy at the Γ point for Bi_2Se_3 are found to be zero within numerical precision, the self-consistently calculated quasiparticle energies must match exactly at the Γ point. We use this fact to rigidly shift the conduction band from the off-diagonal calculation to match the quasiparticle band gap computed when neglecting off-diagonal components, 0.38 eV: $E^{\text{QP}}_{c\mathbf{k}} \approx E^{\text{off-diag}}_{c\mathbf{k}} + (E^{\text{QP, diag}}_{c,\mathbf{k}=\Gamma} - E^{\text{off-diag}}_{c,\mathbf{k}=\Gamma})$. This is expected to be acceptable when the off-diagonal matrix elements of the self-energy for the states away from the Γ point are sufficiently weakly sensitive to corrections to the Kohn-Sham eigenvalues.

As seen in Fig. 4 the conduction and valence bands are now unambiguously parabolic after updating the basis set, so we can readily compute the effective masses. We calculate an effective mass of 0.19 m_e for the holes and 0.14 m_e for the electrons, averaging over the directions plotted. This compares favorably with the experimentally determined effective masses, from magneto-optics, of 0.14 m_e for both the electrons and holes [129]. We note that our determination of effective masses agrees despite the discrepancy in the value of the band gap.

To investigate the sensitivity of the band gap to the treatment of dynamics in the self-energy operator, we also calculate the band gap at the Γ point through the use of the full-frequency treatment of the dielectric function, via the contour deformation method [136] and a low rank approximation [137–139]. We used 15 imaginary frequencies, 200 eigenvectors in a reduced basis scheme, corresponding to roughly 10% of the full spectrum, a frequency spacing of 0.25 Ry, with frequencies calculated out to 10 Ry. We found a slightly larger gap than in the Hybertsen-Louie GPP, with a value of 0.41 eV. In conventional semiconductors, redistribution of the weight of the screening from a single frequency typically results in a lower gap; the increase of the gap for Bi_2Se_3 relative to the GPP result is understood as a consequence of the inverted nature of the band structure. The small change in the value indicates that the use of a GPP model for the dynamics in the self-energy is sufficiently accurate for quasiparticle energies.

We can compare our FR-*GW* calculations of the band structure to a GW+SOC calculation[44] performed with BerkeleyGW. The band gap in *GW*+SOC is found to be direct at Γ, with a value of 0.33 eV, with parabolic valence and conduction bands. (See Table XI for computational details.) In all FR-*GW* cases, the quasiparticle band gap is found to be in a range between 0.38 to 0.41 eV, depending on the treatment of the frequency-dependence of the self-energy operator, and an update to the quasiparticle basis set is required to recover parabolic bands for the valence band maximum and conduction band minimum. Unlike the perturbative *GW*+SOC approach, FR-*GW* more readily allows for a quasiparticle self-consistent approach to arrive at a quasiparticle basis set in which the dependence on qualitatively inaccurate starting-point mean-field bands is removed.

TABLE X. The spin-orbit splitting at the valence band maximum and the change of band gap upon inclusion of spin-orbit coupling for Si and GaAs, in comparison to results computed in the code WEST [50].

	$\Delta^{\text{SOC}}(\Gamma, v)$ (eV)		$E_g^{\text{FR}} - E_g^{\text{SR}}$ (eV)		E_g (eV)
	FR-LDA	FR-*GW*	DFT	*GW*	FR-*GW*
Si, present	0.047	0.049	−0.016	−0.016	1.22
Si, Ref. [50]	0.048	0.049	−0.016	−0.017	1.36
GaP, present	0.089	0.086	−0.027	−0.024	2.57
GaP, Ref. [50]	0.083	0.092	−0.028	−0.031	1.91
GaAs, present	0.320	0.340	−0.098	−0.109	1.49
GaAs, Ref. [50]	0.328	0.344	−0.136	−0.123	0.13

IV. COMPARISON WITH OTHER IMPLEMENTATIONS

Other excited-state *GW* codes have implemented compatibility with spinor wave functions, including pseudopotential plane-wave codes WEST [50] and YAMBO [51], pseudopotential PAW codes VASP [54] and GPAW [53], and all-electron codes FHIAIMS [52], QUESTAAL [75], TURBOMOLE [74], and SPEX [36,49]. At present, only YAMBO [51,55] and BerkeleyGW have BSE with spinor wave functions implemented. We compare our present results with these other implementations, as a first attempt at benchmarking spinorial *GW* and *GW*/BSE calculations in the spirit of the GW100 set [58] and the community effort to examine reproducibility of G_0W_0 calculations in solids [140]. For the standard semiconductors Si, GaP (parameters in Table I), and GaAs, we find good agreement (in Table X) with the computed spin-orbit splitting at the valence band maximum as computed in Ref. [50], despite that work's use of different pseudopotentials from the SG15 database [141] with PBE exchange-correlation functionals [142]. The differences between the present calculations and that of WEST for GaAs are larger than that of Si and GaP due to the considerable underestimation of the direct band gap for GaAs at the SR-*GW* level computed in Ref. [50] using pseudopotentials from the SG15 database (0.62 eV), compared to that from the pseudo-Dojo database (1.26 eV), a discrepancy not present in their results for Si and GaP. Also apparent in Table X is agreement in the shifts of the band gaps upon inclusion of spin-orbit coupling to tens of meV. Results were not found in the literature for FR-*GW*/BSE calculations of these materials

TABLE XI. Comparison between present FR-*GW* and other excited-state calculations from the literature for the bulk band gap for Bi_2Se_3. PW = plane wave, PSP = pseudopotential, GPP = generalized plasmon pole, GN = Godby-Needs plasmon pole, and CD = contour deformation.

	Structure	SOC Treatment	Basis Set	XC Functional	Grid, Polarization	Grid, Self-energy	No. Empty States	Frequency Dependence	Band Gap (eV)
present	expt.	FR-*GW*	PW PSP	LDA	$8\times8\times8$	$8\times8\times8$	1254	GPP	0.38
Ref. [44]	expt.	GW+SOC	PW PSP	LDA	$6\times6\times6$	$6\times6\times6$	∼500	GPP	0.36
Ref. [144]	relaxed	FR-*GW*	PW PSP	PBE	$6\times6\times6$	$6\times6\times6$	3000	GN	0.36
Ref. [127]	expt.	FR-*GW*	FLAPW	LDA	$4\times4\times4$	$4\times4\times4$	300	CD	0.34
Ref. [83]	expt.	FR-*GW*	FLAPW	LDA	$4\times4\times4$	$4\times4\times4$	500	CD	0.20
Ref. [83]	expt.	GW+SOC	FLAPW	LDA	$4\times4\times4$	$4\times4\times4$	500	CD	0.01
Ref. [128]	expt.	FR-*GW*	PW/Gaussian PSP	LDA	$8\times8\times8$	nonuniform[a]	234	GN	0.20

[a] $10\times10\times1$ to $78\times78\times1$.

as a comparison. YAMBO's spin-orbit implementation paper [73] shows results on 2D transition-metal dichalcogenides only, and YAMBO results for GaSb are available only as an unconverged tutorial example [143].

Several results have been reported in the literature for the bulk quasiparticle band gap for Bi_2Se_3, from both *GW*+SOC and FR-*GW* approaches. The *GW* implementation in YAMBO [51,73], a plane-wave pseudopotential excited-state code that computes the polarizability and self-energy with sums over empty states, is most directly comparable to BerkeleyGW, and we find good agreement for our computed FR-*GW* results for the band gap in the diagonal approximation: 0.36 eV from Ref. [144], and 0.38 eV, present work. The quasiparticle band structure in Ref. [144] suggests a direct gap at Γ, though the resolution is not fine enough to determine if the bands have a parabolic dispersion. The present calculation of the band gap differs only by 20 meV from a prior calculation using BerkeleyGW employing the "*GW*+SOC" approach [44], in which spin-orbit coupling was added perturbatively after evaluating quasiparticle energies that neglected spin. The band structure reported in Ref. [128] uses pseudopotentials without semicore Bi orbitals, with both Gaussian orbital and plane-wave basis sets in separate calculations. This band structure is computed with a nonuniform sampling of the Brillouin zone for evaluation of self-energy matrix elements, up to $78\times78\times1$ near the zone center, featuring a direct gap of 0.20 eV and valence band maximum at the Γ point with a flattened parabolic shape. FR-*GW* FLAPW calculations [83,127] using the SPEX [36,49] code show a sensitivity to the band gap to calculation parameters at both the DFT and GW levels. Changing the number of local orbitals from 1 [127] to 2 [83], l_{max} for GW from 4 [127] to 5 [83], the plane-wave cutoff for GW from 3.5 $bohr^{-1}$ [127] to 2.9 $bohr^{-1}$[83], and number of empty states from 300 [83] to 500 [127] changes the band gap from 0.34 to 0.20 eV. By contrast, a perturbative *GW*+SOC calculation [83] with FLAPW found a vanishing band gap, and the bands appeared to become linear, unexpected for the bulk material. To conclude, different descriptions of the wave functions for Bi_2Se_3 can give a direct band gap from about 0.2 to 0.35 eV, with these values within about 0.1 eV of experimental values [127,129,131]. Further study regarding self-consistent updates to the quasiparticle wave functions within the plane-wave pseudopotential FR-*GW* approach can elucidate the features of the bands near the Fermi energy responsible for this sensitivity, and more clarity on the disagreement from ARPES [127] and transmissivity measurements [129] is needed. A comparison between these Bi_2Se_3 calculations is presented in Table XI.

V. PERFORMANCE

We give a comparison in the performance of BerkeleyGW for the representative case of GaAs with and without spinor wave functions. We see in Table XII that the calculation of the wave functions for the self-energy matrix elements ("DFT coarse") takes four times longer, in accordance with expectation from having to double the number of bands and double the size of each wave function, for the spin-up and spin-down components. The calculation of the wave functions for the basis of the BSE Hamiltonian ("DFT fine") is more rapid, since the bottleneck in generating these wave functions is the number of k points and not the number of bands. Calculation of the dielectric matrix ("EPSILON") sees an increase in cost of only 2.5, far less than the increase in cost of generating the matrix elements alone, because the matrix inversion step is a significant fraction of runtime, and it is unaffected by spinors since the size of the dielectric matrix is the same when including or disregarding spin. The calculation of quasiparticle energies ("SIGMA"), however, is closer to the expected increase in cost, at a factor of 4.1. The costs of constructing the BSE kernel ("KERNEL") and solving the eigenvectors and eigenvalues ("ABSORPTION") have the largest increases, at 6.4 and 15.0, respectively. The KERNEL code requires the calculation of three sets of matrix elements, an increase in cost partially offset by time spent on the better-scaling routines such as I/O. We discuss the ABSORPTION code performance in more detail below.

The ABSORPTION code has four main routines: I/O, interpolation of the quasiparticle energies, interpolation of the kernel matrix elements, and diagonalization. We see the performance of each when disregarding spin and when using spinor wave functions in Table XIII. The I/O necessarily has an increase in cost of a factor of 4, from the increase in the size of the wave function files. Similarly, the interpolation of the quasiparticle energies takes nearly 4 times longer, for the same reason. The interpolation of the kernel matrix elements increases cost by a factor of 10.1, less than an estimated increase of 16, since the interpolation coefficients have been calculated in the previous step, and the multiplication with the kernel matrix elements is performed as an optimized matrix-

TABLE XII. Comparison of performance of BerkeleyGW on GaAs, when disregarding spin and when using spinor wave functions.

Step	No. CPUs	CPU Hours (no spin)	CPU Hours (spinor)	Ratio
DFT coarse	1024	162	650	4.0
DFT fine	1728	173	490	2.8
EPSILON	864	864	2160	2.5
SIGMA	864	2760	11232	4.1
KERNEL	600	560	3600	6.4
ABSORPTION	600	48	720	15.0

matrix multiplication with the level 3 BLAS call ZGEMM [57]. The diagonalization sees an increased cost by a factor of 56.8, close to the expected factor of 64.

VI. CONCLUSION

Our implementation of spinor *GW*/BSE in the BerkeleyGW excited-state software enables computation of the quasiparticle energies and absorption spectra for materials with large SOC. The use of DFT one-particle wave functions with two spinor components necessarily increases the cost of calculation, found in practice to be at best about three times more expensive than when neglecting SOC, and with the calculations necessary for calculating the optical absorption within the *GW*/BSE being much more expensive due to the increase in basis set size. The careful use of symmetry however can significantly reduce the cost in some systems.

We demonstrated our implementation on the test systems Si, Ge, GaAs, GaSb, CdSe, and Au, which were readily calculated in the band-diagonal, one-shot G_0W_0 method. The band gaps, spin-orbit splittings, and energy eigenvalues were shown to be highly accurate across this range of different spin-orbit coupling strengths. The band gaps were also shown to be well-approximated when introducing SOC as a perturbation to the valence band maxima computed while neglecting spin. The topological insulator material Bi_2Se_3, however, needed some correction to the LDA basis for the quasiparticle states. While a fairly accurate band gap of 0.38 eV was computed within band-diagonal G_0W_0, the band structure shows small but unphysical features in a small neighborhood about the Γ point. We demonstrated that correcting the LDA basis states by diagonalizing the G_0W_0 Hamiltonian was able to remove this unphysical feature, and provide effective masses in good agreement with experiment.

We additionally performed fully relativistic Bethe-Salpeter equation calculations of the absorption spectra for GaAs and GaSb. We show that the absorption spectrum for GaAs is similar within both the SR-*GW*/BSE and FR-*GW*/BSE. For GaSb, we are able to resolve the spin-orbit split E_1 and $E_1 + \Delta$ peaks, with their placement within tens of meV of experiment.

The perturbative treatment of spin-orbit coupling for electronic structure, *GW*+SOC, shows high agreement with the more costly nonperturbative FR-*GW* approach for many test systems. Such systems, even with nominally strong spin-orbit coupling as in GaSb and Au, have fully relativistic DFT band structures that have high-qualitative agreement with that from FR-*GW*. However, for materials such as Bi_2Se_3 that possess both a narrow band gap and strong spin-orbit coupling, the significant qualitative differences between the fully relativistic DFT band structures and FR-*GW* motivate the use of the FR-*GW* approach. GW+SOC approaches for Bi_2Se_3 have shown conflicting qualitative descriptions of the bulk band gap [44,83], while the FR-*GW* approaches [83,127,128,144] have been consistent, within about 0.1 eV. Further, the use of FR-*GW* allows for updating the quasiparticle wave functions, which then gives good quantitative agreement with the experimentally measured effective masses for electrons (0.14 m_e, experiment [129] and computed and holes (0.14 m_e, experiment [129] and 0.19 m_e, computed) for Bi_2Se_3. The use of FR-*GW*/BSE for the test systems of GaAs and GaSb considered presently gives no significant advantage [62] over the perturbative approach [145], and results on monolayer transition metal dichalcogenides in the literature also show agreement to a few 10 meV between the nonperturbative and perturbative inclusion of SOC in the *GW*/BSE excitonic binding energies [55]. However, it is reasonable to think that in materials where SOC gives a qualitative difference in band structure, like Bi_2Se_3, there may be stronger effects in BSE not captured by a perturbative treatment.

The availability of spinor *GW*/BSE calculations in BerkeleyGW opens the way to increased use of fully relativistic quasiparticle and excitonic absorption calculations in the electronic structure community, enabling more accurate and detailed exploration of topological materials which have garnered great recent research interest, as well as in thermoelectric and photovoltaic materials. BerkeleyGW has particular strengths for large and reduced-dimensional systems, such as a defect in a 2D topological material [146]. Further developments include the use of magnetic group symmetries to facilitate the computation of noncollinear magnetic systems without the requirement of large supercells [73], and the calculation of noncollinear spin susceptibilities [72], as well as more benchmarking FR-*GW*/BSE for materials with large spin-orbit coupling and large exciton binding energies. We find good agreement with other existing *GW* implementations, and believe that further detailed comparison can help

TABLE XIII. Comparison of performance of ABSORPTION executable in BerkeleyGW when disregarding spin and when using spinor wave functions, as seen in calculations of GaAs.

Step	Wall time, no spin (s)	Wall time, spinor (s)	Ratio
I/O	138	560	4.0
Interp. WFN	57	240	4.2
Interp. Kernel	27	274	10.1
Diag.	53	3013	56.8

to improve implementations of this methodology and ensure accuracy.

This implementation of spinor *GW*/BSE in BerkeleyGW was publicly released in BGW version 3.0, and a tutorial example for performing *GW*/BSE calculations is available in Ref. [147].

ACKNOWLEDGMENTS

The authors would like to thank Felipe H. da Jornada, Derek Vigil-Fowler, Georgy Samsonidze, Gabriel Antonius, Tonatiuh Rangel, and Jeffrey B. Neaton for productive discussions. The authors would also like to thank Jamal Mustafa for sharing the private PYTHON repository for CMS-PY, scripts for computing quasiparticle Fermi energies for metals, used for the quasiparticle band structure for Au. This work was supported by National Science Foundation Grant No. DMR10-1006184 and by the Office of Science, Office of Basic Energy Sciences, U.S. Department of Energy: by the Director of the Materials Sciences and Engineering Division under Contract No. DE-AC02-05CH11231, within the Nanomachines Program (KC1203) and within the Theory of Materials Program (KC2301), as well as from the CTC and CPIMS Programs, under Award No. DE-SC0019053. Computational resources have been provided by the DOE at Lawrence Berkeley National Laboratory's NERSC facility.

[1] V. Tshitoyan, J. Dagdelen, L. Weston, A. Dunn, Z. Rong, O. Kononova, K. A. Persson, G. Ceder, and A. Jain, Unsupervised word embeddings capture latent knowledge from materials science literature, Nature (London) **571**, 95 (2019).

[2] L.-D. Zhao, J. He, D. Berardan, Y. Lin, J.-F. Li, C.-W. Nan, and N. Dragoe, BiCuSeO oxyselenides: New promising thermoelectric materials, Energy Environ. Sci. **7**, 2900 (2014).

[3] Y. Pei, H. Wang, and G. J. Snyder, Band engineering of thermoelectric materials, Adv. Mater. **24**, 6125 (2012).

[4] J. R. Sootsman, D. Y. Chung, and M. G. Kanatzidis, New and old concepts in thermoelectric materials, Angew. Chem. Int. Ed. **48**, 8616 (2009).

[5] G. Chen, M. S. Dresselhaus, G. Dresselhaus, J.-P. Fleurial, and T. Caillat, Recent developments in thermoelectric materials, Int. Mater. Rev. **48**, 45 (2003).

[6] D. Zhao and G. Tan, A review of thermoelectric cooling: materials, modeling and applications, Appl. Therm. Eng. **66**, 15 (2014).

[7] D.-Y. Chung, T. P. Hogan, M. Rocci-Lane, P. Brazis, J. R. Ireland, C. R. Kannewurf, M. Bastea, C. Uher, and M. G. Kanatzidis, A new thermoelectric material: $CsBi_4Te_6$, J. Am. Chem. Soc. **126**, 6414 (2004).

[8] C. Wood, Materials for thermoelectric energy conversion, Rep. Prog. Phys. **51**, 459 (1988).

[9] F. D. M. Haldane, Model for a Quantum Hall Effect without Landau Levels: Condensed-Matter Realization of the "Parity Anomaly", Phys. Rev. Lett. **61**, 2015 (1988).

[10] C. L. Kane and E. J. Mele, Quantum Spin Hall Effect in Graphene, Phys. Rev. Lett. **95**, 226801 (2005).

[11] M. Z. Hasan and C. L. Kane, Colloquium: topological insulators, Rev. Mod. Phys. **82**, 3045 (2010).

[12] J. E. Moore, The birth of topological insulators, Nature (London) **464**, 194 (2010).

[13] L. Fu, C. L. Kane, and E. J. Mele, Topological Insulators in Three Dimensions, Phys. Rev. Lett. **98**, 106803 (2007).

[14] M. König, S. Wiedmann, C. Brüne, A. Roth, H. Buhmann, L. W. Molenkamp, X.-L. Qi, and S.-C. Zhang, Quantum spin Hall insulator state in HgTe quantum wells, Science **318**, 766 (2007).

[15] B. A. Bernevig, T. L. Hughes, and S.-C. Zhang, Quantum spin Hall effect and topological phase transition in HgTe quantum wells, Science **314**, 1757 (2006).

[16] S. Murakami, N. Nagaosa, and S.-C. Zhang, Spin-Hall Insulator, Phys. Rev. Lett. **93**, 156804 (2004).

[17] Y. Ando, Topological insulator materials, J. Phys. Soc. Jpn. **82**, 102001 (2013).

[18] X. Wan, A. M. Turner, A. Vishwanath, and S. Y. Savrasov, Topological semimetal and Fermi-arc surface states in the electronic structure of pyrochlore iridates, Phys. Rev. B **83**, 205101 (2011).

[19] A. A. Burkov and L. Balents, Weyl Semimetal in a Topological Insulator Multilayer, Phys. Rev. Lett. **107**, 127205 (2011).

[20] B. Q. Lv, H. M. Weng, B. B. Fu, X. P. Wang, H. Miao, J. Ma, P. Richard, X. C. Huang, L. X. Zhao, G. F. Chen, Z. Fang, X. Dai, T. Qian and H. Ding, Experimental Discovery of Weyl Semimetal TaAs, Phys. Rev. X **5**, 031013 (2015).

[21] H. Weng, C. Fang, Z. Fang, B. A. Bernevig, and X. Dai, Weyl Semimetal Phase in Noncentrosymmetric Transition-Metal Monophosphides, Phys. Rev. X **5**, 011029 (2015).

[22] Z. Liu, B. Zhou, Y. Zhang, Z. Wang, H. Weng, D. Prabhakaran, S.-K. Mo, Z. Shen, Z. Fang, X. Dai *et al.*, Discovery of a three-dimensional topological Dirac semimetal, Na_3Bi, Science **343**, 864 (2014).

[23] F. Schindler, A. M. Cook, M. G. Vergniory, Z. Wang, S. S. Parkin, B. A. Bernevig, and T. Neupert, Higher-order topological insulators, Sci. Adv. **4**, eaat0346 (2018).

[24] Y. Tanaka, Z. Ren, T. Sato, K. Nakayama, S. Souma, T. Takahashi, K. Segawa, and Y. Ando, Experimental realization of a topological crystalline insulator in SnTe, Nat. Phys. **8**, 800 (2012).

[25] N. J. Jeon, J. H. Noh, Y. C. Kim, W. S. Yang, S. Ryu, and S. I. Seok, Solvent engineering for high-performance inorganic–organic hybrid perovskite solar cells, Nat. Mater. **13**, 897 (2014).

[26] B.-W. Park, B. Philippe, X. Zhang, H. Rensmo, G. Boschloo, and E. M. J. Johansson, Bismuth based hybrid perovskites A3Bi2I9 (A: Methylammonium or Cesium) for solar cell application, Adv. Mater. **27**, 6806 (2015).

[27] K. Frohna, T. Deshpande, J. Harter, W. Peng, B. A. Barker, J. B. Neaton, S. G. Louie, O. M. Bakr, D. Hsieh, and M. Bernardi, Inversion symmetry and bulk Rashba effect in methylammonium lead iodide perovskite single crystals, Nat. Commun. **9**, 1829 (2018).

[28] W. Kohn and L. J. Sham, Self-consistent equations including exchange and correlation effects, Phys. Rev. **140**, A1133 (1965).

[29] P. Hohenberg and W. Kohn, Inhomogeneous electron gas, Phys. Rev. **136**, B864 (1964).
[30] L. Hedin and S. Lundqvist, Effects of electron-electron and electron-phonon interactions on the one-electron states of solids, Solid State Phys. **23**, 1 (1970).
[31] M. S. Hybertsen and S. G. Louie, Electron correlation in semiconductors and insulators: Band gaps and quasiparticle energies, Phys. Rev. B **34**, 5390 (1986).
[32] M. Rohlfing and S. G. Louie, Electron-hole excitations and optical spectra from first principles, Phys. Rev. B **62**, 4927 (2000).
[33] E. Kaxiras and J. D. Joannopoulos, *Quantum Theory of Materials* (Cambridge University Press, 2019).
[34] L. D. Landau and L. M. Lifshitz, *Quantum Mechanics: Non-Relativistic Theory* (Pergamon Press, 1977).
[35] K. V. Shanavas, Z. S. Popović, and S. Satpathy, Theoretical model for Rashba spin-orbit interaction in *d* electrons, Phys. Rev. B **90**, 165108 (2014).
[36] R. Sakuma, C. Friedrich, T. Miyake, S. Blügel, and F. Aryasetiawan, GW calculations including spin-orbit coupling: Application to Hg chalcogenides, Phys. Rev. B **84**, 085144 (2011).
[37] B. K. Bhattacharyya, D. M. Bylander, and L. Kleinman, Comparison of fully relativistic energy bands and cohesive energies of $MoSi_2$ and WSi_2, Phys. Rev. B **32**, 7973 (1985).
[38] A. Rajagopal, Inhomogeneous relativistic electron gas, J. Phys. C: Solid State Phys. **11**, L943 (1978).
[39] A. H. MacDonald and S. Vosko, A relativistic density functional formalism, J. Phys. C: Solid State Phys. **12**, 2977 (1979).
[40] M. S. Hybertsen and S. G. Louie, Spin-orbit splitting in semiconductors and insulators from the ab initio pseudopotential, Phys. Rev. B **34**, 2920 (1986).
[41] L. A. Hemstreet, C. Y. Fong, and J. S. Nelson, First-principles calculations of spin-orbit splittings in solids using nonlocal separable pseudopotentials, Phys. Rev. B **47**, 4238 (1993).
[42] B. D. Malone and M. L. Cohen, Quasiparticle semiconductor band structures including spin-orbit interactions, J. Phys.: Condens. Matter **25**, 105503 (2013).
[43] T. Rangel, D. Kecik, P. E. Trevisanutto, G.-M. Rignanese, H. Van Swygenhoven, and V. Olevano, Band structure of gold from many-body perturbation theory, Phys. Rev. B **86**, 125125 (2012).
[44] O. V. Yazyev, E. Kioupakis, J. E. Moore, and S. G. Louie, Quasiparticle effects in the bulk and surface-state bands of Bi_2Se_3 and Bi_2Te_3 topological insulators, Phys. Rev. B **85**, 161101(R) (2012).
[45] E. Kioupakis, M. L. Tiago, and S. G. Louie, Quasiparticle electronic structure of bismuth telluride in the GW approximation, Phys. Rev. B **82**, 245203 (2010).
[46] H. Zhang, C.-X. Liu, X.-L. Qi, X. Dai, Z. Fang, and S.-C. Zhang, Topological insulators in Bi_2Se_3, Bi_2Te_3 and Sb_2Te_3 with a single Dirac cone on the surface, Nat. Phys. **5**, 438 (2009).
[47] S. Biering and P. Schwerdtfeger, A comparative density functional study of the high-pressure phases of solid ZnX, CdX, and HgX (X= S, Se, and Te): Trends and relativistic effects, J. Chem. Phys. **137**, 034705 (2012).
[48] B. A. Barker and S. G. Louie, The electronic structure of β-HgS via *GW* calculations, arXiv:2203.15831.
[49] C. Friedrich, S. Blügel, and A. Schindlmayr, Efficient implementation of the GW approximation within the all-electron FLAPW method, Phys. Rev. B **81**, 125102 (2010).
[50] P. Scherpelz, M. Govoni, I. Hamada, and G. Galli, Implementation and Validation of Fully Relativistic GW Calculations: Spin-Orbit Coupling in Molecules, Nanocrystals, and Solids, J. Chem. Theory Comput. **12**, 3523 (2016).
[51] A. Marini, C. Hogan, M. Grüning, and D. Varsano, YAMBO: an ab initio tool for excited state calculations, Comput. Phys. Commun. **180**, 1392 (2009).
[52] M. Kühn and F. Weigend, One-electron energies from the two-component GW method, J. Chem. Theory Comput. **11**, 969 (2015).
[53] T. Deilmann, Valley selectivity induced by magnetic adsorbates: Triplet oxygen on monolayer MoS_2, Phys. Rev. B **101**, 085130 (2020).
[54] G. Kresse and J. Furthmüller, Efficient iterative schemes for ab initio total-energy calculations using a plane-wave basis set, Phys. Rev. B **54**, 11169 (1996).
[55] M. Marsili, A. Molina-Sánchez, M. Palummo, D. Sangalli, and A. Marini, Spinorial formulation of the *GW*/BSE equations and spin properties of excitons in two-dimensional transition metal dichalcogenides, Phys. Rev. B **103**, 155152 (2021).
[56] K. Lejaeghere, G. Bihlmayer, T. Björkman, P. Blaha, S. Blügel, V. Blum, D. Caliste, I. E. Castelli, and S. J. Clark, Reproducibility in density functional theory calculations of solids, Science **351**, aad3000 (2016).
[57] J. Deslippe, G. Samsonidze, D. A. Strubbe, M. Jain, M. L. Cohen, and S. G. Louie, BerkeleyGW: A massively parallel computer package for the calculation of the quasiparticle and optical properties of materials and nanostructures, Comput. Phys. Commun. **183**, 1269 (2012).
[58] M. J. van Setten, F. Caruso, S. Sharifzadeh, X. Ren, M. Scheffler, F. Liu, J. Lischner, L. Lin, J. R. Deslippe, S. G. Louie, C. Yang, F. Weigend, J. B. Neaton, F. Evers, and P. Rinke, GW100: Benchmarking G_0W_0 for molecular systems, J. Chem. Theory Comput. **11**, 5665 (2015).
[59] M. Del Ben, F. H. da Jornada, A. Canning, N. Wichmann, K. Raman, R. Sasanka, C. Yang, S. G. Louie, and J. Deslippe, Large-scale GW calculations on pre-exascale HPC systems, Comput. Phys. Commun. **235**, 187 (2019).
[60] F. H. da Jornada, D. Y. Qiu, and S. G. Louie, Nonuniform sampling schemes of the brillouin zone for many-electron perturbation-theory calculations in reduced dimensionality, Phys. Rev. B **95**, 035109 (2017).
[61] B. A. Barker, Electronic and optical properties of solids with strong spin-orbit coupling, Ph.D. thesis, University of California, Berkeley, 2018.
[62] M. L. Cohen and J. R. Chelikowsky, *Electronic Structure and Optical Properties of Semiconductors* (Springer Science & Business Media, 2012), Vol. 75.
[63] J.-L. Li, G.-M. Rignanese, E. K. Chang, X. Blase, and S. G. Louie, GW study of the metal-insulator transition of bcc hydrogen, Phys. Rev. B **66**, 035102 (2002).
[64] E. Młyńczak, I. Aguilera, P. Gospodarič, T. Heider, M. Jugovac, G. Zamborlini, J.-P. Hanke, C. Friedrich, Y. Mokrousov, C. Tusche, S. Suga, V. Feyer, S. Blügel, L. Plucinski, and C. M. Schneider, Fe(001) angle-resolved photoemission and intrinsic anomalous Hall conductivity in Fe

seen by different ab initio approaches: LDA and GGA versus *GW*, Phys. Rev. B **105**, 115135 (2022).
[65] J.-L. Li, G.-M. Rignanese, and S. G. Louie, Quasiparticle energy bands of NiO in the GW approximation, Phys. Rev. B **71**, 193102 (2005).
[66] F. Aryasetiawan and O. Gunnarsson, Electronic Structure of NiO in the *GW* Approximation, Phys. Rev. Lett. **74**, 3221 (1995).
[67] X. Zhu and A. W. Overhauser, Plasmon-pole and paramagnon-pole model of an electron liquid, Phys. Rev. B **33**, 925 (1986).
[68] C. A. Kukkonen and A. W. Overhauser, Electron-electron interaction in simple metals, Phys. Rev. B **20**, 550 (1979).
[69] J. Lischner, T. Bazhirov, A. H. MacDonald, M. L. Cohen, and S. G. Louie, Effect of spin fluctuations on quasiparticle excitations: First-principles theory and application to sodium and lithium, Phys. Rev. B **89**, 081108(R) (2014).
[70] F. Aryasetiawan and S. Biermann, Generalized Hedin's Equations for Quantum Many-Body Systems with Spin-Dependent Interactions, Phys. Rev. Lett. **100**, 116402 (2008).
[71] E. Şaşıoğlu, A. Schindlmayr, C. Friedrich, F. Freimuth, and S. Blügel, Wannier-function approach to spin excitations in solids, Phys. Rev. B **81**, 054434 (2010).
[72] D. Nabok, S. Blügel, and C. Friedrich, Electron–plasmon and electron–magnon scattering in ferromagnets from first principles by combining GW and GT self-energies, npj Comput. Mater. **7**, 178 (2021).
[73] D. Sangalli, A. Ferretti, H. Miranda, C. Attaccalite, I. Marri, E. Cannuccia, P. Melo, M. Marsili, F. Paleari, A. Marrazzo *et al.*, Many-body perturbation theory calculations using the YAMBO code, J. Phys.: Condens. Matter **31**, 325902 (2019).
[74] C. Holzer and W. Klopper, Ionized, electron-attached, and excited states of molecular systems with spin–orbit coupling: Two-component GW and Bethe–Salpeter implementations, J. Chem. Phys. **150**, 204116 (2019).
[75] A. Vishina, Fully relativistic Green's functions method, Ph.D. thesis, King's College London, 2019.
[76] See Supplemental Material at http://link.aps.org/supplemental/10.1103/PhysRevB.106.115127 for the derivation of one-particle excitations from many-body perturbation theory including spin-orbit coupling, details on symmetries with spinor wave functions, figures of band structures, figure of the absorption spectrum of GaAs, details regarding the convergence of the quasiparticle band structure of Bi_2Se_3, and quasiparticle energies of Au computed with the Godby-Needs Plasmon Pole model.
[77] K. Karlsson and F. Aryasetiawan, Spin-wave excitation spectra of nickel and iron, Phys. Rev. B **62**, 3006 (2000).
[78] G. Theurich and N. A. Hill, Self-consistent treatment of spin-orbit coupling in solids using relativistic fully separable ab initio pseudopotentials, Phys. Rev. B **64**, 073106 (2001).
[79] S. L. Adler, Quantum theory of the dielectric constant in real solids, Phys. Rev. **126**, 413 (1962).
[80] N. Wiser, Dielectric constant with local field effects included, Phys. Rev. **129**, 62 (1963).
[81] A. Fleszar, Dielectric response in semiconductors: Theory and applications, Ph.D. thesis, University of Trieste, 1985.
[82] I. W. Bulik, G. Scalmani, M. J. Frisch, and G. E. Scuseria, Noncollinear density functional theory having proper invariance and local torque properties, Phys. Rev. B **87**, 035117 (2013).
[83] I. Aguilera, C. Friedrich, and S. Blügel, Spin-orbit coupling in quasiparticle studies of topological insulators, Phys. Rev. B **88**, 165136 (2013).
[84] P. Y. Yu and M. Cardona, *Fundamentals of Semiconductors: Physics and Materials Properties*, Graduate Texts in Physics (Springer, Berlin, 2010).
[85] M. L. Cohen and S. G. Louie, *Fundamentals of Condensed Matter Physics* (Cambridge University Press, 2016).
[86] D. R. Hamann, Generalized norm-conserving pseudopotentials, Phys. Rev. B **40**, 2980 (1989).
[87] G. Onida, L. Reining, and A. Rubio, Electronic excitations: density-functional versus many-body Green's-function approaches, Rev. Mod. Phys. **74**, 601 (2002).
[88] T. Rangel, S. M. Hamed, F. Bruneval, and J. B. Neaton, An assessment of low-lying excitation energies and triplet instabilities of organic molecules with an ab initio Bethe-Salpeter equation approach and the Tamm-Dancoff approximation, J. Chem. Phys. **146**, 194108 (2017).
[89] M. Shao, F. H. da Jornada, C. Yang, J. Deslippe, and S. G. Louie, Structure preserving parallel algorithms for solving the Bethe-Salpeter eigenvalue problem, Linear Algebra Appl. **488**, 148 (2016).
[90] S. W. Shepperd, Quaternion from rotation matrix, J. Guid. Control **1**, 223 (1978).
[91] F. L. Markley and G. M. Lerner, Three-Axis Attitude Determination Methods, in *Spacecraft Attitude Determination and Control*, edited by J. R. Wertz (Kluwer, Boston, 1978), pp. 410–435.
[92] F. L. Markley, Unit quaternion from rotation matrix, J. Guid. Control. Dyn. **31**, 440 (2008).
[93] M. Tinkham, *Group Theory and Quantum Mechanics*, International Series in Pure and Applied Physics (McGraw-Hill Book Company, 1964).
[94] K. H. Hellwege and O. Madelung, *Numerical Data and Functional Relationships in Science and Technology*, Landolt Börnstein, New Series, Group III, Vol. 17a and 22a (Springer, 1982).
[95] O. Madelung, *Semiconductors: Data Handbook* (Springer, Berlin, Heidelberg, 2004).
[96] J. P. Perdew and A. Zunger, Self-interaction correction to density-functional approximations for many-electron systems, Phys. Rev. B **23**, 5048 (1981).
[97] D. R. Hamann, Optimized norm-conserving Vanderbilt pseudopotentials, Phys. Rev. B **88**, 085117 (2013).
[98] M. van Setten, M. Giantomassi, E. Bousquet, M. Verstraete, D. Hamann, X. Gonze, and G.-M. Rignanese, The PseudoDojo: Training and grading a 85 element optimized norm-conserving pseudopotential table, Comput. Phys. Commun. **226**, 39 (2018).
[99] M. L. Tiago, S. Ismail-Beigi, and S. G. Louie, Effect of semicore orbitals on the electronic band gaps of Si, Ge, and GaAs within the GW approximation, Phys. Rev. B **69**, 125212 (2004).
[100] P. Giannozzi, S. Baroni, N. Bonini, M. Calandra, R. Car, C. Cavazzoni, D. Ceresoli, G. L. Chiarotti, M. Cococcioni, I. Dabo, A. D. Corso, S. de Gironcoli, S. Fabris, G. Fratesi, R. Gebauer, U. Gerstmann, C. Gougoussis, A. Kokalj, M. Lazzeri, L. Martin-Samos *et al.*, QUANTUM ESPRESSO: A modular and open-source software project for quantum simulations of materials, J. Phys.: Condens. Matter **21**, 395502 (2009).

[101] I. P. Rusinov, I. A. Nechaev, and E. V. Chulkov, Theoretical study of influencing factors on the dispersion of bulk band-gap edges and the surface states in topological insulators Bi_2Te_3 and Bi_2Se_3, J. Exp. Theor. Phys. **116**, 1006 (2013).

[102] S. B. Zhang, D. Tománek, M. L. Cohen, S. G. Louie, and M. S. Hybertsen, Evaluation of quasiparticle energies for semiconductors without inversion symmetry, Phys. Rev. B **40**, 3162 (1989).

[103] R. W. Godby and R. J. Needs, Metal-Insulator Transition in Kohn-Sham Theory and Quasiparticle Theory, Phys. Rev. Lett. **62**, 1169 (1989).

[104] P. Larson, M. Dvorak, and Z. Wu, Role of the plasmon-pole model in the GW approximation, Phys. Rev. B **88**, 125205 (2013).

[105] J. Deslippe, G. Samsonidze, M. Jain, M. L. Cohen, and S. G. Louie, Coulomb-hole summations and energies for GW calculations with limited number of empty orbitals: A modified static remainder approach, Phys. Rev. B **87**, 165124 (2013).

[106] J. I. Mustafa, M. Bernardi, J. B. Neaton, and S. G. Louie, Ab initio electronic relaxation times and transport in noble metals, Phys. Rev. B **94**, 155105 (2016).

[107] M. Cardona, N. E. Christensen, and G. Fasol, Relativistic band structure and spin-orbit splitting of zinc-blende-type semiconductors, Phys. Rev. B **38**, 1806 (1988).

[108] P. E. Blöchl, O. Jepsen, and O. K. Andersen, Improved tetrahedron method for Brillouin-zone integrations, Phys. Rev. B **49**, 16223 (1994).

[109] J. Mustafa, cmspy-unreleased PYTHON software (2017).

[110] S. Zollner, M. Garriga, J. Humlicek, S. Gopalan, and M. Cardona, Temperature dependence of the dielectric function and the interband critical-point parameters of GaSb, Phys. Rev. B **43**, 4349 (1991).

[111] P. Romaniello and P. de Boeij, The role of relativity in the optical response of gold within the time-dependent current-density-functional theory, J. Chem. Phys. **122**, 164303 (2005).

[112] P. B. Johnson and R. W. Christy, Optical Constants of the Noble Metals, Phys. Rev. B **6**, 4370 (1972).

[113] I.-B. Lin, T. W.-H. Sheu, and J.-H. Li, Effects of exchange correlation functional on optical permittivity of gold and electromagnetic responses, Opt. Express **22**, 30725 (2014).

[114] M. Cardona and M. L. W. Thewalt, Isotope effects on the optical spectra of semiconductors, Rev. Mod. Phys. **77**, 1173 (2005).

[115] M. Cardona, Electron-phonon interaction in tetrahedral semiconductors, Solid State Commun. **133**, 3 (2005).

[116] D. R. Masovic, F. R. Vukajlovic, and S. Zekovic, Local-pseudopotential calculation for optical properties and photoemission valence-band spectrum of silicon, J. Phys. C: Solid State Phys. **16**, 6731 (1983).

[117] P. Lautenschlager, M. Garriga, S. Logothetidis, and M. Cardona, Interband critical points of GaAs and their temperature dependence, Phys. Rev. B **35**, 9174 (1987).

[118] S. S. Vishnubhatla and J. C. Woolley, Reflectance spectra of some III-V compounds in the vacuum ultraviolet, Can. J. Phys. **46**, 1769 (1968).

[119] K. A. Mills, R. F. Davis, S. D. Kevan, G. Thornton, and D. A. Shirley, Angle-resolved photoemission determination of Λ-line valence bands in Pt and Au using synchrotron radiation, Phys. Rev. B **22**, 581 (1980).

[120] A. Baalmann, M. Neumann, H. Neddermeyer, W. Radlik, and W. Braun, Bandstructure of gold and copper: A synchrotron radiation study, Ann. Israeli Phys. Soc. **6**, 351 (1983).

[121] R. Courths, H. G. Zimmer, A. Goldmann, and H. Saalfeld, Electronic structure of gold: An angle-resolved photoemission study along the Λ line, Phys. Rev. B **34**, 3577 (1986).

[122] R. C. Jaklevic and L. C. Davis, Band signatures in the low-energy-electron reflectance spectra of fcc metals, Phys. Rev. B **26**, 5391 (1982).

[123] P. Szczepanek and R. Glosser, Piezo-optical constants of gold, Solid State Commun. **15**, 1425 (1974).

[124] R. C. Jaklevic and J. Lambe, Experimental study of quantum size effects in thin metal films by electron tunneling, Phys. Rev. B **12**, 4146 (1975).

[125] A.-B. Chen and B. Segall, Piezooptical response associated with the interconduction band transitions in the noble metals, Solid State Commun. **18**, 149 (1976).

[126] D. Marel, G. Sawatzky, R. Zeller, F. Hillebrecht, and J. Fuggle, Unoccupied band critical point energies of noble metals determined with Bremsstrahlung isochromat spectroscopy, Solid State Commun. **50**, 47 (1984).

[127] I. A. Nechaev, R. C. Hatch, M. Bianchi, D. Guan, C. Friedrich, I. Aguilera, J. L. Mi, B. B. Iversen, S. Blügel, P. Hofmann, and E. V. Chulkov, Evidence for a direct band gap in the topological insulator Bi_2Se_3 from theory and experiment, Phys. Rev. B **87**, 121111(R) (2013).

[128] T. Förster, P. Krüger, and M. Rohlfing, Two-dimensional topological phases and electronic spectrum of Bi_2Se_3 thin films from G W calculations, Phys. Rev. B **92**, 201404(R) (2015).

[129] M. Orlita, B. A. Piot, G. Martinez, N.K.S. Kumar, C. Faugeras, M. Potemski, C. Michel, E. M. Hankiewicz, T. Brauner, Č. Drašar, S. Schreyeck, S. Grauer, K. Brunner, C. Gould, C. Brüne, and L. W. Molenkamp, Magneto-Optics of Massive Dirac Fermions in Bulk Bi_2Se_3, Phys. Rev. Lett. **114**, 186401 (2015).

[130] I. Aguilera, C. Friedrich, G. Bihlmayer, and S. Blügel, GW study of topological insulators Bi_2Se_3, Bi_2Te_3, and Sb_2Te_3: Beyond the perturbative one-shot approach, Phys. Rev. B **88**, 045206 (2013).

[131] S. Kim, M. Ye, K. Kuroda, Y. Yamada, E. E. Krasovskii, E. V. Chulkov, K. Miyamoto, M. Nakatake, T. Okuda, Y. Ueda, K. Shimada, H. Namatame, M. Taniguchi, and A. Kimura, Surface Scattering via Bulk Continuum States in the 3D Topological Insulator Bi_2Se_3, Phys. Rev. Lett. **107**, 056803 (2011).

[132] M. van Schilfgaarde, T. Kotani, and S. Faleev, Quasiparticle Self-Consistent GW Theory, Phys. Rev. Lett. **96**, 226402 (2006).

[133] T. Kotani, M. van Schilfgaarde, and S. V. Faleev, Quasiparticle self-consistent G W method: A basis for the independent-particle approximation, Phys. Rev. B **76**, 165106 (2007).

[134] M. Shishkin, M. Marsman, and G. Kresse, Accurate Quasiparticle Spectra from Self-Consistent *GW* Calculations with Vertex Corrections, Phys. Rev. Lett. **99**, 246403 (2007).

[135] W. Chen and A. Pasquarello, Accurate band gaps of extended systems via efficient vertex corrections in GW, Phys. Rev. B **92**, 041115(R) (2015).

[136] R. W. Godby, M. Schlüter, and L. J. Sham, Self-energy operators and exchange-correlation potentials in semiconductors, Phys. Rev. B **37**, 10159 (1988).

[137] R. Car, E. Tosatti, S. Baroni, and S. Leelaprute, Dielectric band structure of crystals: General properties and calculations for silicon, Phys. Rev. B **24**, 985 (1981).

[138] M. Govoni and G. Galli, Large scale GW calculations, J. Chem. Theory Comput. **11**, 2680 (2015).

[139] M. Del Ben, F. H. da Jornada, G. Antonius, T. Rangel, S. G. Louie, J. Deslippe, and A. Canning, Static subspace approximation for the evaluation of G_0W_0 quasiparticle energies within a sum-over-bands approach, Phys. Rev. B **99**, 125128 (2019).

[140] T. Rangel, M. Del Ben, D. Varsano, G. Antonius, F. Bruneval, F.H. da Jornada, M. J. van Setten, O. K. Orhan, D. D. O'Regan, A. Canning *et al.*, Reproducibility in G0W0 calculations for solids, Comput. Phys. Commun. **255**, 107242 (2020).

[141] M. Schlipf and F. Gygi, Optimization algorithm for the generation of ONCV pseudopotentials, Comput. Phys. Commun. **196**, 36 (2015).

[142] J. P. Perdew, K. Burke, and M. Ernzerhof, Generalized Gradient Approximation Made Simple, Phys. Rev. Lett. **77**, 3865 (1996).

[143] D. Sangalli, YAMBO Wiki: SOC, http://www.yambo-code.org/wiki/index.php?title=SOC (2015).

[144] A. Lawal, A. Shaari, R. Ahmed, and N. Jarkoni, First-principles many-body comparative study of Bi_2Se_3 crystal: A promising candidate for broadband photodetector, Phys. Lett. A **381**, 2993 (2017).

[145] D. Y. Qiu, F.H. da Jornada, and S. G. Louie, Optical Spectrum of MoS_2: Many-Body Effects and Diversity of Exciton States, Phys. Rev. Lett. **111**, 216805 (2013).

[146] M. Chrobak, K. Maćkosz, M. Jurczyszyn, M. Dobrzański, K. Nowak, T. Ślezak, M. Zając, M. Sikora, M. Rams, T. Eelbo *et al.*, Fe dopants and surface adatoms versus nontrivial topology of single-crystalline Bi_2Se_3, New J. Phys. **22**, 063020 (2020).

[147] https://workshop.berkeleygw.org/tutorial-workshop-resources/about.